Analysis of Vortex Generators

Department of
Wind Energy
Master Report

Antonios Charalampous Papageorgiou

DTU Wind Energy-M-0158

August 2017

DTU Wind Energy
Department of Wind Energy

Authors: Antonios Charalampous Papageorgiou
Title: Analysis of Vortex Generators

DTU Wind Energy-M-0158
August 2017

Project Period:
January – August 2017

ECTS: 35

Education: Master of Science

Supervisors:

Martin O. L. Hansen
DTU Wind Energy

Clara Marika Velte
DTU Mechanical Engineering

Remarks:
This report is submitted as partial fulfillment of the requirements for graduation in the above education at the Technical University of Denmark.

DTU Wind Energy is a department of the Technical University of Denmark with a unique integration of research, education, innovation and public/private sector consulting in the field of wind energy. Our activities develop new opportunities and technology for the global and Danish exploitation of wind energy. Research focuses on key technical-scientific fields, which are central for the development, innovation and use of wind energy and provides the basis for advanced education at the education.

We have more than 240 staff members of which approximately 60 are PhD students. Research is conducted within nine research programmes organized into three main topics: Wind energy systems, Wind turbine technology and Basics for wind energy.

Technical University of Denmark
Department of Wind Energy
Frederiksborgvej 399
4000 Roskilde
Denmark
www.vindenergi.dtu.dk

List of Abbreviations

AEP Annual Energy Production

CAD Computer-Aided Design

CFD Computational Fluid Dynamics

CoE Cost of Energy

DNS Direct Numerical Simulation

k-ω SST k-ω Shear Stress Transport Turbulence Model

LML Laboratoire de Mécanique de Lille

LOV Lamb-Oseen Vortex

RANS Reynolds-Averaged Navier-Stokes

ReD Rectangular devices referring to VGs

Re Reynolds number

RST Reynolds Stress Transport Turbulence Model

SPIV Stereoscopic Particle Image Velocimetry

TI Turbulence Intensity

TrD Triangular devices referring to VGs

VG Vortex Generator

Nomenclature

β VG angle of incidence to the oncoming flow [°]

$\Delta\theta$ Angular segment for the line integration $[rad]$

ϵ Vortex core diameter $[m]$

Γ Circulation of the velocity field $[\frac{m^2}{sec}]$

λ Spanwise period for ReD and TrD configurations [m]

ν Kinematic viscosity of air $[\frac{m^2}{sec}]$

ρ	Air density $[\frac{kg}{m^3}]$
d_f	Distance between the edges of the floor and the far vanes $[m]$
d_{IN-VG}	Distance between the velocity inlet and the leading edges of the vanes $[m]$
d_{VG-OUT}	Distance between the trailing edges of the vanes and the pressure outlet $[m]$
dz_{exp}	Experimental grid step $[m]$
dz_{num}	Numerical grid step $[m]$
F	Net pressure force $[\frac{N}{m}]$
h	Height of VG $[m]$
L	Distance between the trailing edges of the vanes [m]
l	Lift force $[\frac{N}{m}]$
L_{VG}	Length of VG $[m]$
L_{WT}	Length of the wind tunnel floor $[m]$
P	Pressure distribution along VGs length $[Pa]$
r	Radius for the line integration $[m]$
r_ϵ	Vortex core radius $[m]$
U	Incoming streamwise velocity $[\frac{m}{sec}]$
u_x	Lateral velocity component (Hypothesis chapter) $[\frac{m}{sec}]$
u_x	Streamwise velocity component (Results & Validation chapters) $[\frac{m}{sec}]$
u_y	Streamwise velocity component (Hypothesis chapter) $[\frac{m}{sec}]$
u_y	Vertical velocity component (Results & Validation chapters) $[\frac{m}{sec}]$
u_z	Lateral velocity component (Results & Validation chapters) $[\frac{m}{sec}]$
u_z	Vertical velocity component (Hypothesis chapter) $[\frac{m}{sec}]$
u_θ	Tangential velocity $[\frac{m}{sec}]$
w	Width of VG $[m]$

Abstract

Vortex generators (VGs) is a commonly used aerodynamic device consisting of small vanes which are placed on the wind turbine blades. The vortices created behind the VGs produce momentum mixing between the region near the wall and the free stream region which delays the local flow separation and thus aerodynamic stall. This is important near the blade root of the blades where thick airfoils with poor aerodynamic properties are required in order to carry the large in plane bending moment. The implementation of VGs in these airfoils allows the chord to decrease proportionally to the increase in the lift coefficient. Therefore, a more slender and thereby a cheaper blade can be produced.

The generated flow behind the VGs can be investigated with the use of CFD modelling. A widely used method is the specification of body forces acting on the air near the VGs which induces a realistic flowfield that can be solved in a computational grid. This is called the BAY model. However, a numerical model which fully resolves the geometry of the VGs should be more accurate since no prior assumptions on the body forces are required. In this research, two numerical models which resolve the rectangular and the triangular geometries of VGs are built in order to test the induced flow behavior behind these vanes. The computational grid consists of 11.3 10^6 cells for the rectangular devices and 8.2 10^6 for the triangular devices. The three Transport Turbulence models that are tested are: k-ω SST, Spalart-Allmaras, Reynolds-Stress. The generated flow behind the devices are compared to PIV data in various downstream planes. The main indicator for the validation procedure is the circulation of the velocity field which is calculated directly from its definition and with the use of the Lamb-Oseen Vortex. The Reynolds-Stress model is the one that provides the most accurate comparison between the numerical and experimental results. Furthermore, a hypothesis for the VGs case is verified as for conventional wings. Specifically, the circulation in the wake is estimated as the summation of trailed circulation from the lifting line theory and the bound circulation is calculated with the use of Kutta-Joukowski airfoil theory even if the aspect ratio is really low. The lift force is calculated as the integrated pressure difference along the VGs height. The successful results of testing this hypothesis in the rectangular VGs were presented by M.O.L Hansen in the Wind Energy Science Conference 2017 (WESC2017). The abstract was categorized in the Mini Symposia: 'M7-Advances in Design of Large Wind Turbine Rotors' and the presentation took place on Monday the 26th of June, 2017. The presentation can be seen in Appendix E.

Preface

This report is submitted in partial fulfillment of the requirements for acquiring the degree of Master of Science (M.Sc.) in Wind Energy. This research was conducted during the Spring semester of 2017 under the guidance of my supervisors, Associate Professor Martin Otto Laver Hansen from the Department of Wind Energy and Associate Professor Clara Marika Velte from the Department of Mechanical Engineering.

The present thesis has been composed by the author and complies with DTU regulations on plagiarism. However, a part of the text is based on research of others. The best has been done in order to provide precise references in these sources.

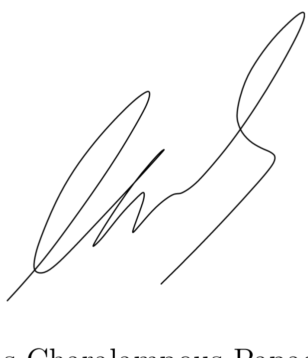

Antonios Charalampous-Papageorgiou
Kongens Lyngby, August 2017

Acknowledgements

Hereby, I would like to express my gratitude to my supervisors; Associate Professor Martin Otto Laver Hansen and Associate Professor Clara Marika Velte for the unstintingly knowledge that they provided and their willingness to help in every problem that I encountered with. Their constant guidance allowed me to distinguish the targets of this research and acquire a solid understanding of the scientific concepts. Also, the experimental data that they shared with me is a key part of this thesis.

Furthermore, I would like to thank my friends, Sayantan and Vaggelis, for providing me a such suitable environment to write my thesis in 404 data bar and being such an inspiring company. Finally, I want to thank my parents, Victoria and Lampros, for doing everything they could in order for me to fulfill my dreams.

Contents

List of Figures

List of Tables

1. Introduction

In this part, the main idea as well as the purpose of this research are introduced. The objectives are illustrated and the scope of this thesis is briefly discussed. Finally, the content of this report is provided to the reader in order to follow the sequence of the chapters.

1.1. General context

Nowadays, the necessity to cover society's ever increasing energy needs from renewable energy sources is apparent. The rapid growth of the wind energy industry is a consequent of this requirement. However, many steps towards improvement are still required, so that wind energy can become more competitive in the energy market. Therefore, increasing of the annual energy production for a given rotor design (AEP) is crucial since this is an important parameter of the cost of energy (CoE). An accurate method for calculating this cost can be found in [5] and is equal to the investment cost plus the discounted maintenance cost divided by the discounted production measured in kWh over the lifetime period i.e 20 years. This relation allows the scientists and the manufacturers to explore new ways and methods, either to reduce the wind turbine cost i.e applying new materials, improving production efficiency and/or to optimize the AEP. Thus, a continuing quest for improved wind turbine aerodynamic performance exists since it is one of the fundamental aspects which could contribute to the establishment of the wind energy as a major part of the energy market.

The engineering developments in aerodynamics lead to efficient and smart design with enhanced performance. The addition of vortex generators (VGs) to the blades is potentially one of the simplest and most cost-effective methods for increasing the AEP in both planned and existing wind turbines [6]. These add-ons are defined as VGs since they induce vortices in the downstream region of the flow. Typically, they are small vanes with relatively simple geometry, projecting normal to the surface at a certain angle of attack of the incoming flow so that they behave like half wings [6]. The fundamental principle relies on the mix of momentum near the wall, with high momentum flow from the free-stream region. In simple terms, VGs act as the intermediates between the high-energy region i.e free stream and the region close to the walls where separations appears, by producing 'swirls'. In this case, the flow attachment is much longer which is crucial since the flow separation causes momentum losses. These losses have as a result the increase of drag and the aggravation of the airfoil performance.

The advantages that VGs offer are not only applicable to wind turbine blades but also to various engineering applications where control of boundary layer and reattachment is desired. For instance, the surfaces of a fin-and-tube heat exchanger could be enhanced by using VGs as presented in [7] or the aerodynamic drag of a car could be reduced as described in [8]. VGs were apparently first used in the early '50s by H.D Taylor at United Aircraft [9]. Since then, numerous approaches have been made in order to determine which VG parameters have a major influence on the flow and the aerodynamic performance [10]. Detailed experimental campaigns [1],[11],[12] were accomplished and various ways of modelling VGs were implemented in order to investigate and verify the behavior of the induced vortices generated from them. For instance, the BAY model which uses source terms in the momentum equation enforcing flow tangency is extensively being used in the industry [13],[14]. However, a numerical model resolving the full geometry of VG itself should be more precise since no prior assumptions on the force distribution is needed on a realistic body. Thus, the aim of this research is to examine how well the flow past the VGs is resolved when a direct numerical model is used.

1.2. Purpose

As aforementioned in 1.1, the main purpose of this research is to build a numerical model that fully resolves the geometry of VGs. The commercial CFD software used for this investigation is STAR CCM+ and it is licensed by CD-adapco. Specifically, two different geometries of VGs, rectangular (ReD) and triangular (TrD), are integrated and tested, consisting of four individual vanes. Multiple mesh grids are generated and evaluated but only the two most sufficient and less computational expensive are provided in this report. To validate the performance of the numerical model, experimental data are thoroughly investigated and compared to the computational results. The experimental data are obtained using the Particle Image Velocimetry (PIV) method as it is analytically described in [1]. The numerical computations are extracted in various planes in the downstream area of the VGs and fundamental parameters such as circulation Γ are selected in order to validate the numerical model's performance by comparing the outcome with the experimental results. Three different turbulence models are implemented and verified. The latter purpose is to examine a hypothesis for the VGs similarly to the wings of finite span. In the steady ideal flow case that is investigated, the bound circulation is calculated from the 2D airfoil theory and the correlation with the circulation in the wake is examined with the use of the lifting line theory. The derived results of this hypothesis are then compared with the experimental and computational wake circulation coming from definition and the Lamb-Oseen Vortex. This hypothesis produces significant conclusions on how well the vortex generators behave as conventional wings even though the aspect ratio is low.

1.3. Objectives

It can be stated that the three main objectives of this thesis are:

- Build two numerical models that fully resolve the rectangular and triangular geometries of VGs. Evaluate the generated flow in the wake region by comparing to PIV data.
- Estimate the circulation with the direct use of definition and with the use of Lamb-Oseen Vortex.

- Investigate the correlation between the circulation in the wake and the bound circulation as on conventional wings.

1.4. Scope

The novelty of this research lies in the existence of experimental data really close to the VGs which facilitate the functionality of the numerical model [15]. This relies on the fact that is significantly effortless to achieve a fine mesh discretization close to the VGs in order to test the accuracy of the numerical model. However, the limited computational resources of the personal computer used for this research do not allow to generate a similar mesh far from the vanes. Thus, lower quality results may be produced further into the wake. This means that a sufficient overall analysis with minimized discrepancies between the investigated areas requires a personal computer with a larger RAM memory and more core-CPUs. In addition, the time restrictions required for the fulfillment of this report, allowed three different turbulence models to be implemented and only the steady state case to be tested. For the second purpose of this report which is the verification of the lifting line hypothesis for the VGs, a large amount of pressure data need to be extracted from STAR-CCM+. This procedure could be more accurate and optimized regarding the time by applying various field functions and macro-commands. For instance in the case of the triangular VGs, the extraction procedure could be enhanced since the coordinates on the geometry are identified manually. adding uncertainties in the results. This may add uncertainty on the results. Thus, this report works as a guideline based on a preliminary research which creates the conditions for further analysis.

1.5. Layout

The structure of the present report is the following:

- At first, a brief description of the experimental set up of [1] is provided since the creation of the numerical model is based on it.
- The steps followed in numerical modelling are presented as well as the limitations of the model.
- The numerical results for both rectangular and triangular configurations are illustrated and compared qualitatively to the experimental results.
- The model is further investigated and validated by analyzing the production of circulation in the wake using the definition and the Lamb Oseen Vortex for both experimental and computational data.
- The correlation between the bound and the trailed circulation is examined as on conventional wings.
- The outcome of this research is further discussed and some conceptions for future work are proposed.

2. Background

To examine the generated flow past the VGs, an experiment campaign was conducted in the Laboratoire de Mécanique de Lille (LML) wind tunnel facility, located in Lille, France. The full experiment can be found in [1], but for the purpose of the numerical modelling some parameters and important information are provided. In Figure 2.1, the side and top view of LML wind tunnel is shown. The test section is 20 m long and allows for a 30 cm boundary layer leading to an accurate and detailed investigation of the flow physics [1].

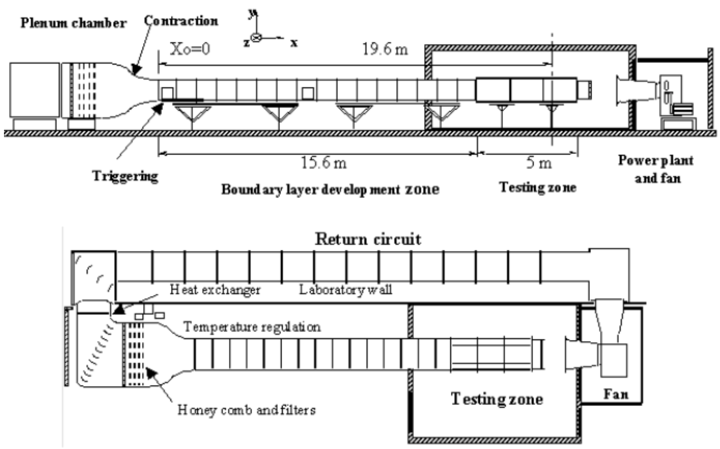

Figure 2.1: Side and top view of the LML boundary layer wind tunnel [1]

The two investigated devices are the rectangular and the triangular. They have identical height and length equal to $h = 0.06m$ and $L_{VG} = 2h$, respectively. A simple sketch of the investigated devices is provided in Figure 2.2.

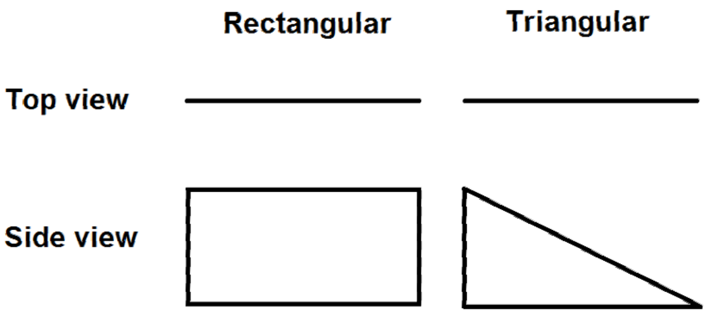

Figure 2.2: Investigated VG geometries [1]

It is important to mention some more device parameters for the formation and study of the numerical model but also for the generic operation of VGs. In Figure 2.3 the VG angle, β, can be seen. For this investigation, this angle remains constant and equal to 18°. This parameter is called the angle of incidence and it is unique in any installation arrangement and directly associated with an optimal model and analysis [10]. The span-wise period λ, is equal to $6h$ and the distance L, between the trailing edges is equal to $2.5h$. Both ReD and TrD configurations are set up with vanes of counter-rotating type in order to produce counter-rotating vortices. Particularly, the four vanes are placed in pairs with an alternate stagger sign in the angle of incidence β, producing vortices of alternate direction.

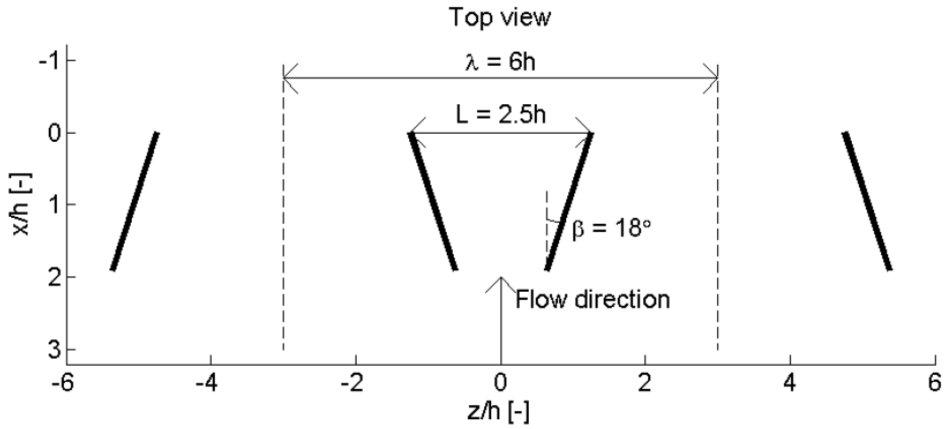

Figure 2.3: Top view of VGs installation arrangement [1]

The boundary layer in this case is turbulent and the Reynolds number (Re) is the basic indicator for the flow regime:

$$Re = \frac{U \cdot L_{Re}}{\nu} \tag{2.1}$$

The stream-wise velocity component in the velocity inlet is set equal to 8 $[\frac{m}{sec}]$ and the kinematic viscosity of air, ν, to $1.51 \cdot 10^{-5}$ $[\frac{m^2}{sec}]$. The characteristic length for the Re calculation L_{Re} is identical to L_{VG}. Therefore, it can be derived that the Re based on the characteristic length L_{Re} is approximately 64000.

In the present measurements campaign, the instantaneous in-plane velocity components and the stream-wise i.e out of plane velocity are extracted in five different planes for the ReD and in two planes for the TrD . The plane sections are normal to the flow and a large Stereoscopic Particle Image Velocity (SPIV) is used in order to obtain the results. All the realizations obtained from PIV are averaged with a common origo as C M Velte states in [1]. Table 2.1 summarizes the position for each measurement plane as a function of VG height for both ReD and TrD configurations in the downstream region of interest.

Table 2.1: Measurements planes in the downstream region of VGs

	Measurements planes		
Planes positions	Downstream distance in [m]	ReD	TrD
3h	0.18	✓	✓
12h	0.72	✓	✓
25h	1.5	✓	-
40h	2.4	✓	-
50h	3	✓	-

Consequently, the flow generated by the numerical model will be investigated in these downstream planes.

3. Numerical model

In this chapter, the gradual procedure of creating the numerical model is provided having as main purpose to help the reader follow all the required steps. At first, the basic information about the design parameters of CAD/geometry for both rectangular and triangular configurations is provided as well as the different concepts that were applied are shown. Also, the boundary conditions assigned to each region are explained and the mesh grids generated for both rectangular and triangular are analyzed. Finally, the three turbulence models: k-ω SST, Reynolds Stress and Spalart-Allmaras implemented for this study are illustrated along with the corresponding physics models for each case.

3.1. CAD/Geometry for rectangular and triangular devices

The commercial software STAR-CCM+ used for this thesis gives the opportunity to build the geometry within its own environment. Thus, the geometry parts for the two configurations are created and assembled with the fully integrated CAD tool. As presented in the previous section the set up consists of two small pairs of fins attached to the floor of the wind tunnel. Even if the concept of the design seems simple, differences exist between the construction of the two models i.e ReD, TrD, making the numerical modelling not a trivial procedure.

In the case of ReD configuration, the first step is to create a sketch of a two-dimensional profile on a planar surface [3]. This planar surface resembles the LML wind tunnel floor used for the experiment and it is presented in Figure 3.1 below:

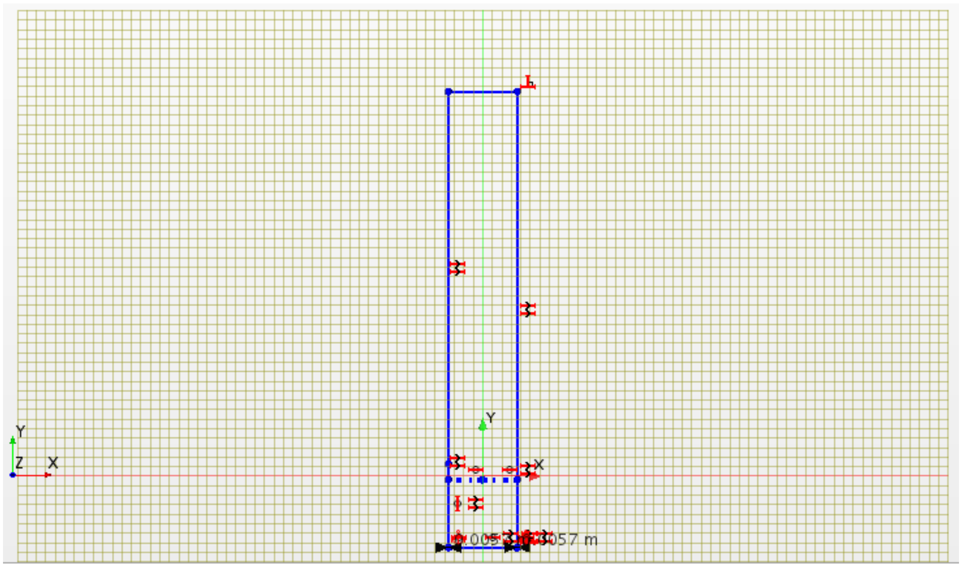

Figure 3.1: Design of the simulated wind tunnel floor

Figure 3.2 illustrates a second sketch of the overall geometry. It consists of four individual rectangular sketches that correspond to the positions of the four VGs. The dimensioning procedure is accomplished by taking into account the experimental configuration shown in Figure 2.3.

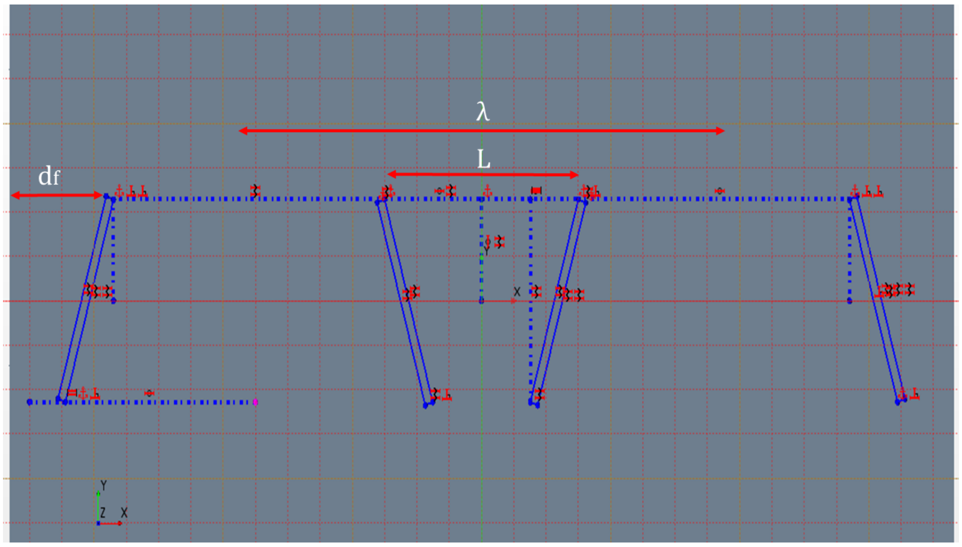

Figure 3.2: Preliminary sketch for the rectangular vanes

The distance between the edges of the floor and the far vanes,d_f, is the only one not obtained from the aforementioned Figure 2.3. Therefore, it is estimated equal to $\frac{L}{2}$ i.e distance between the y-axis and the edges of the middle VG pair. Table 3.1 includes all the necessary information about the dimensions of the preliminary XY sketch. Apparently, the coordinate system used in the numerical simulations has a different orientation compared to the experimental set up (see Figure 2.3). However, this is an insignificant issue as the results will be presented with identical coordinate axes.

Table 3.1: Dimensioning of the rectangular CAD/Geometry

coordinate system	x y z	Lateral direction Stream-wise direction Vertical direction	[m]
VG parameters	h	VG height	0.06
	L_{VG}	VG length	0.12
	w	VG width	0.01
	L	Distance between the trailing edges	0.15
	λ	Spanwise period	0.36
	d_f	Distance between the sides of the tunnel and the far vanes	0.075
	d_{IN-VG}	Distance between the velocity inlet (IN) and the leading edges of the vanes (VG)	3.72
	d_{VG-OUT}	Distance between the trailing edges of the vanes (VG) and the pressure outlet (OUT)	3.2

To convert the 2D sketch into a complete 3D/CAD model, one more step is required. The extrusion tool provided by the software extends the draft rectangles of Figure 3.2 into the investigated configuration of Figure 3.3:

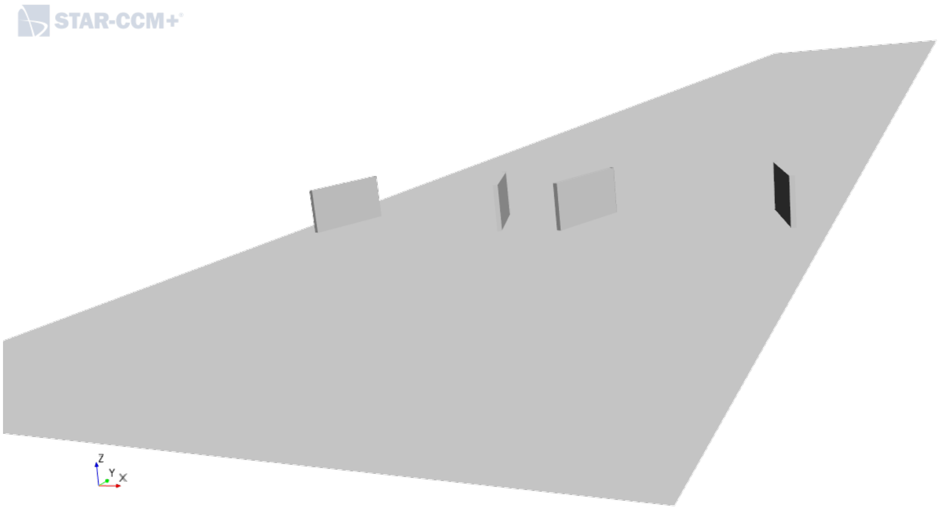

Figure 3.3: Geometry scene of the rectangular configuration

It is obvious that for the rectangular devices the extrusion is applied in the z-direction and it is equal to the VG height. However, this could not be implemented in the triangular devices. Thus, the design for the second numerical model is based on four different planes, normal to the simulated floor and rotated to 18° i.e angle of incidence. In this case, the extruded part is equal to the VG's width ,w, as it is shown in Figure 3.4.

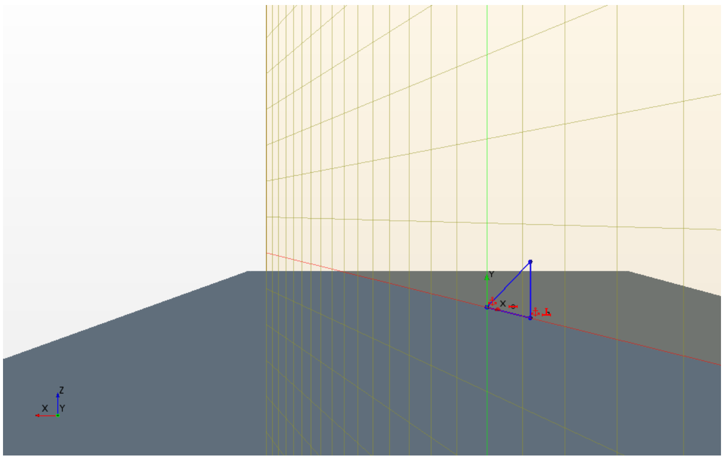

Figure 3.4: Preliminary sketch for the triangular vanes

There is no need to define new dimensions for the triangular devices since they are the same as the ones presented above in Table 3.1. The only design parameter that differs in this set up is the d_{VG-OUT} which is set equal to 1.3 m. The integrated configuration of the rectangular vanes could be seen in Appendix A (see Figure A.1).

The last geometry parts that must be constructed are the surrounding walls of the wind tunnel floor. A rectangular block of 0.4 m height (z-direction) is created as it can be found in Appendix A (see Figure A.2).

3.1.1. Critical design parameters

There are two critical design parameters in this investigation:

- The first one is the distance between the velocity inlet and the leading edges of the VGs (d_{IN-VG}). It is crucial to allow the velocity profile to develop in order to form a similar flow regime with the one presented in [1]. Therefore, a parametric analysis of this distance is conducted and the stream-wise velocity profiles of the upstream area, close to the VGs are extracted and investigated. The outcome of this analysis is presented before the illustration of the results (section 3.5).
- The distance between the trailing edges of the VGs and the pressure outlet d_{VG-OUT} is the second most critical parameter since is highly correlated with the volume mesh discretization and the convergence of the solution. Thus, the final selection of this length is a decision made after an iterative process which is also presented in the end of this chapter (section 3.5).

3.2. Boundary conditions

The next step after creating the geometry for the two configurations is to assign the boundary conditions to the regions. The fluid behavior and the physical properties at all bound surfaces are defined through these boundaries. It is important to set them before the mesh discretization, since some parts of the volume mesh e.g. prism layer mesh which is analyzed in the following chapter, are depended on the type of the boundary. The complete geometry part is split into six regions in order to assign the proper boundary conditions for the problem. The first region corresponds to the velocity inlet boundary, the second one is the pressure outlet condition while in the third and fourth symmetry planes are applied as boundaries. The wind tunnel floor (fifth region) and the two pairs of VGs (sixth region) are treated as wall boundaries. Figure 3.5 provides an overall visualization of the assigned boundaries to the regions in a mesh scene.

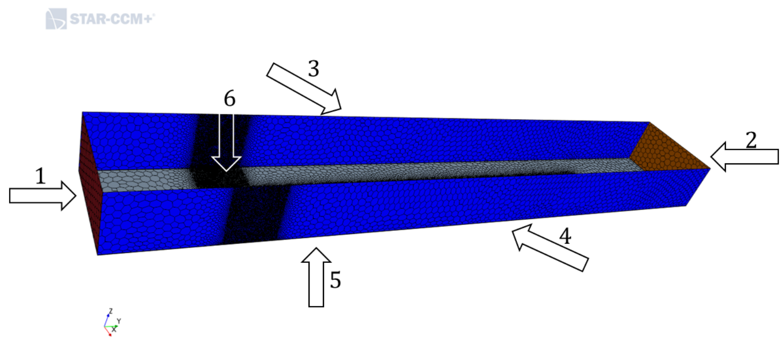

Figure 3.5: Assigned boundaries to each region of geometry

Velocity inlet (Region 1)

A velocity inlet condition is applied to the side of the block that is normal to the floor in the upstream region. The velocity magnitude is defined equal to 8 $\frac{m}{sec}$ and the direction is specified to y axis [0,1,0]. The Turbulence Intensity (TI) and Turbulence Viscosity Ratio are set constant to the default values equal to 0.01 and 10 respectively. As it is mentioned in [3], these values are suitable for a high-quality wind tunnel.

Pressure outlet (Region 2)

Pressure outlet is assigned to the side of the wall normal to the floor in the downstream region. This boundary defines that all gradients of all variables are zero in the flow direction, except pressure. To achieve that, the location of the outlet must be selected far away from all geometrical disturbances in order for the flow to reach a fully developed state where no changes will occur in the flow direction [16].

Symmetry planes (Region 3,4)

Two symmetry planes are assigned to the walls parallel to the stream-wise direction. The velocities normal to the symmetry boundaries are set to zero, and the values of all other variables outside of the domain are equated to their respective values at the nearest node, just inside the domain [16].

Walls (Region 5,6)

The wall is the most common boundary condition in confined fluid flow problems [16] where the relative fluid velocity tangential to the wall is set equal to zero (no-slip). In this case, the two pairs of VGs and the wind tunnel floor are set to this type of boundary.

3.3. Mesh generation

The fluid flow past the VGs is quite complicated and this is the reason why it can be approached only numerically. Thus, in order to analyze it, the 3D flow domain must be split into smaller subdomains created by geometric primitives as tetrahedra or hexahedra. Then, the governing equations describing the fluid flow can be computationally solved using finite volume methods inside these subdomains [17]. It is important to assure continuity between the adjacent faces of the generated cells i.e subdomains, so that the individual solutions inside them will be able to produce an accurate representation of the fluid flow. To minimize the aforementioned issue, a polyhedral mesh grid is generated in STAR CCM+. This meshing option provides a detailed and balanced solution for complicated problems as the one investigated in this study. Moreover, this tool requires less computational power, since it produces five times fewer cells, than the equivalent tetrahedral. In addition, another advantage of this meshing option is that it does not require more surface preparation[3]. A distinct polyhedral cell could be seen in Appendix A (see A.3).

Achieving a satisfying mesh is a procedure that could be characterized as the bottleneck of the entire analysis. It requires continuous visual inspection and engineering judgment by the user, in order to evaluate its quality. One fundamental way to reach high quality mesh is to refine the areas of interest by producing more cells. In this specific investigation, it could be stated that these areas are:

1. The area really close to the investigated geometry i.e close to the VGs
2. The downstream region up to the last plane section where experimental data exist (see Table 2.1)

A top view of the generated mesh including these refined areas can be seen in Figure 3.6. The Figure is obtained from a mesh generation where d_{IN-VG} was set equal to 0.72 m.

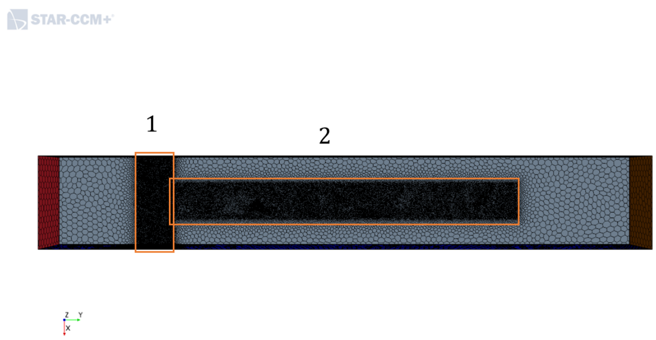

Figure 3.6: Top view of the generated mesh for the ReD configuration

Also, the automated mesh options contribute significantly in the grid quality of the critical regions. For instance, the regions near to the walls where flow separation exists demand a different discretization approach. The most common approach is the implementation of orthogonal prism layers near to boundaries in order to capture the development of the boundary layer. So, a specified amount of these layers are attached to the VGs and to the four walls of the wind tunnel as shown in Figure 3.7.

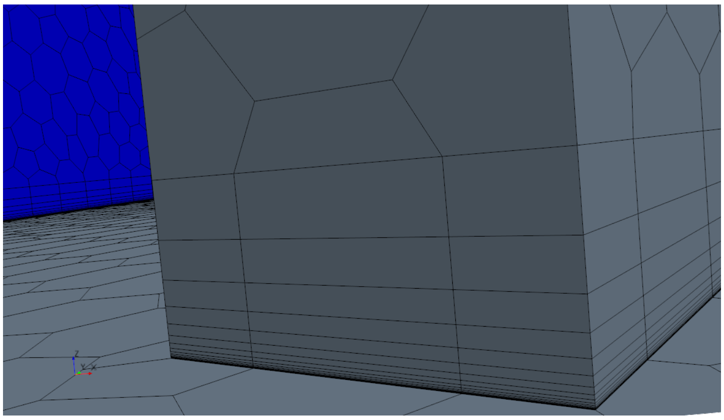

Figure 3.7: Prism layers attached to VGs and surrounding walls

The choice of a sufficient amount of prism layers is a complex and time consuming process since it could affect the results in various ways. A lower than the required amount of layers may let the numerical model work without resulting in the desired solution of the fluid flow. On the other hand, an excessive number of prism layers would not enhance the results compared to a mesh including a sufficient amount.

In order to provide quantitative information for the refined areas and the prism layers, an important parameter needs to be specified in advance. This is the characteristic dimension called Base size, generating the light grey area in Figure 3.6. It could be identical to the diameter of the inlet or the length of the fluid volume [3]. In this case, it is chosen to be equal to 0.05 m. It is a convenient size for scaling the two relative sizes that correspond to the areas of interest i.e close to VGs, wake region. The only restriction for the final refining percentages is the limited computational resources of the system used for this research (see Appendix, A.1).

The TrD mesh generation demands a lower amount of cells compared to the rectangular configuration since the wake region is not required to be fully resolved (see Appendix A, Figure A.4). The reason is that the experimental data are provided up to 12h downstream as mentioned in Table 2.1. Regarding the ReD configuration, the comparison between the numerical and the measured data is conducted further into the wake up to 50h downstream.

Table 3.2 summarizes all the parameters that define the polyhedral and prism layer mesh for the numerical model.

Table 3.2: Mesh properties for the rectangular and triangular devices

Polyhedral mesh	ReD	TrD
Base size [m]	0.05	0.05
Relative size close to VGs [%]	9	8
Relative size in the wake region [%]	11	-
Prism layer mesh		
Number of Prism layers	20	20
Prism layer stretching	1.5	1.5
Prism layer thickness [% of the Base size]	5	5
Total amount of cells	$11.3 \cdot 10^6$	$8.2 \cdot 10^6$

The RAM memory margins are exceeded when slightly lower values are applied on the relative sizes presented in Table 3.2. This happens due to the non linear relation that the increase of the cells flows. For instance, if the relative size percentage close to the VGs for the ReD slightly decrease, the total number of cells will approach a significantly higher amount of values without following a proportionate increase rate. Taking into account the limited RAM memory sources, a sudden termination on the mesh generation could be caused. It would have been beneficial to use a PC with three or four times the amount of cores and the provided RAM memory in order to generate a higher quality discretization and thereby a more realistic outcome.

The CPU time and the number of cores used for the mesh generation are presented in the table below:

Table 3.3: Computational time for both ReD and TrD configurations

	ReD	**TrD**
Number of cores	8	8
CPU time [hh:mm]	5:24	4:12

In table 3.3, it can be seen that the time for the mesh generation is significantly high. A computer with more CPU cores would have allowed to investigate more the mesh discretization and thereby its influence on the numerical model.

3.4. Physics modelling

Computational modelling can be divided in three subcategories. The first one is the Direct Numerical Simulations (DNS) which solves the flow equations in all length and time scales. The second is referred to as scale-resolving simulations and can resolve up to a certain limit of scales [18]. The third and most widely applicable is the Reynolds-Averaged Navier-Stokes (RANS) equations. RANS simulations average all scales without excluding the extra Reynolds stresses on the mean flow due to the velocity fluctuations. To estimate these stresses, turbulence models need to be implemented in RANS equations. The appropriate combination of state and time equations are also required in order to fulfill the definition of the physics continuum. Thus, in this part of the report, all the models and corresponding fluid properties that describe the behavior of the flow are provided.

State

In the cases where the speed of the investigated fluid is low, the density remains constant with a fluid element. In this investigation, the wind speed is equal to $8[\frac{m}{sec}]$ and the flow is considered incompressible with no variable density. The constant value of air density is equal to 1.181415 $[\frac{kg}{m^3}]$.

Type of flow solver

The commercial software used for the simulations provides two methods of flow solving for the incompressible flows. The first one is called segregated or uncoupled and the second is the coupled flow solver. The one applied in this model is the uncoupled flow solver since it requires less memory than the coupled. However, if the Mach number of the flow is above 0.7 only the coupled flow option could solve this particular case.

Time

As mentioned in 1.4, the steady state case is the one investigated in this thesis. Therefore, all the variables which define the flow behavior are unchanging in time [19].

RANS

In the case of the 3D modelling of the VGs, it is obvious that a three dimensional space model is applied. Thus, the flow can be analytically described by Navier-Stokes equations shown below in tensor notation (i,j=1,2,3):

$$\rho(\frac{\partial u_i}{\partial t} + u_j\frac{\partial u_i}{\partial x_j}) = -\frac{\partial p}{\partial x_i} + \frac{\partial}{\partial x_j}(\mu\frac{\partial u_i}{\partial x_j}) + \rho g_i \tag{3.1}$$

where u_i is the mean velocity components in the x_i, p is the mean pressure and ρg_i is the gravity force in the i-th direction. The first component of the equation is zero since a steady state case is examined. Also, the continuity equation is required in order to describe the flow:

$$\frac{\partial u_i}{\partial x_i} = 0 \tag{3.2}$$

The basic parameter that indicates the flow regime in a fluid flow problem is the Re number. As aforementioned, the Re number is approximately 64000 based on the reference length which indicates that the regime is fully turbulent. For this reason, each variable u_i has to be decomposed into a mean or averaged value $\overline{u_i}$ and a fluctuating component u_i' [19]. The decomposition is illustrated in eq.3.3:

$$u_i = \overline{u_i} + u_i' \tag{3.3}$$

The derived equation 3.3 is substituted into equations (3.1) and (3.2) leading to RANS equation:

$$\rho(\overline{u_j}\frac{\partial \overline{u_i}}{\partial x_j}) = -\frac{\partial \overline{p}}{\partial x_i} + \frac{\partial}{\partial x_j}(\mu\frac{\partial \overline{u_i}}{\partial x_j} - \rho\overline{u_i'u_j'}) + \rho\overline{g_i} \tag{3.4}$$

The term $\rho\overline{u_i'u_j'}$ represents the stresses due to fluctuations and are known as Reynolds Stresses. To obtain equations that contain only the mean scales, these terms required to be modelled removing any reference to the fluctuating part of the velocity. This is known as the closure problem and various transport turbulence models are introduced in order to close the RANS equations [3].

3.4.1. Turbulence models

The commercial software offers four classes of RANS turbulence models. In this research, three turbulence models included in these four major groups, are implemented and tested. The dynamics behind the turbulence models are quite complicated and not easy to understand but with the contribution of bibliography a brief explanation for each one of them is provided.

k-ω Shear Stress Transport Model (SST)

In general, the k-ω model is a two equation model that estimates the turbulent viscosity by solving the two equations of turbulent kinetic energy k and the dissipation rate per unit turbulent kinetic energy ω [3]. This model was first introduced by David C. Wilcox and a thorough presentation of it can be found in his book about turbulence modelling [20]. However, F.R. Menter [21] first addressed the sensitivity to the free-stream/inlet conditions that the initial k-ω includes. Therefore, a revised model i.e k-ω SST was produced by F.R. Menter in order to eliminate this disadvantage far from the walls.

This model has been most applied to the aerospace industry [3] and for this reason it is selected to be tested in this investigation.

Reynolds-Stress (RST)

The second model implemented in this analysis is the RST turbulence model. This type is potentially able to predict complex flows since it directly estimates all the added shear stress components of eq.3.4 by solving their governing transport equations [3]. However, this direct resolving contributes significantly to the computational time as six more equations need to be solved in order to estimate the Reynolds Stresses.

Spalart-Allmaras Model

Spalart-Allmaras is also a widely applicable turbulence model in the aerospace industry. In contrast to k-ω SST, this model is a single equation model and determines the turbulent viscosity by solving the transport equation for diffusivity instead of turbulent kinetic energy as addressed in [22].

3.5. Limitations of the numerical model

After fulfilling all the above steps, the numerical simulations are ready to run. However, a significant amount of time is spent in the overall procedure shown in Figure 3.8 in order to propose an optimal combination between the numerical model's limitations and the desirable results.

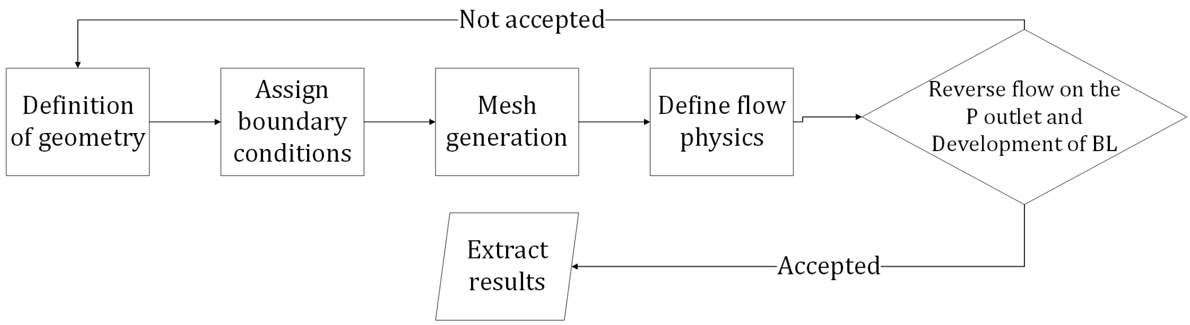

Figure 3.8: Building process of the numerical model

Due to the large mesh size, the execution of the simulation files exceeds the computational capabilities of DTU's personal computers . For this reason, sixteen cores of 'surt fysik' cluster are used in order to achieve the desired results. The simulations are set to stop around seven thousands iterations depending on the investigated turbulence model. For instance, the RST model requires more iteration steps and more computational time for each iteration than the Spalart-Allmaras model. This is mainly caused by the different amount of equations that each model needs to solve in order to converge. During the running procedure, two main issues regarding the mesh generation arise and lead to diverged solutions.

The first one is that the turbulence viscosity increases higher than a limited value in a variable amount of mesh cells in a specific region of the domain. This problem appears due to an insufficient amount of prism layers on the wall boundaries. Therefore an iterative procedure for both ReD and TrD configurations is executed in order to come up with the proper number of prism layers illustrated in Table 3.2.

The second major issue is that the fluid flow reverses on pressure outlet boundary. This can be avoided only if the pressure outlet is placed sufficiently far from the vanes so the flow in the wake is undisturbed. However, an unreasonably long wind tunnel may eliminate the reverse flow problem but it will require many more grid cells leading to RAM memory issues. As aforementioned, the length of d_{VG-OUT} for the ReD is set equal to 3.2 m. On the other hand, it is not required to define such a long length for the TrD configuration since the experimental results exist in two downstream planes(see Table 2.1). Therefore, the d_{VG-OUT} is set equal to 1.3 m. Obviously, this allows a finer mesh for the TrD since the area that needs to be discretized is smaller compared to the ReD.

In an attempt to mimic the flow that C M Velte achieves in [1], a parametric analysis is conducted in the d_{IN-VG} length. An initial guess is to place the VGs 0.72 m downstream of the velocity inlet which corresponds to approximately $12h$. In Figure 3.9 it can be seen that this try leads to a velocity profile that becomes almost constant at the VGs height which obviously is not fully developed yet. This profile is not desirable since the VGs are expected to be placed deeply inside the boundary layer as C M Velte states in [1]. Thus, it is decided to vary the d_{IN-VG} and its' influence on the boundary layer thickness is observed in Figure 3.9. Even though a high discrepancy still lies between the experimental data shown in [1] and all investigated velocity profiles, it is decided to continue the analysis with the d_{IN-VG} equal to 3.72 m which is the most sufficient compared to the other three cases. This is the highest elongation that can be achieved with these computational resources. A larger extrusion could be achieved but it demands a coarser mesh discretization in order to avoid exceeding RAM memory limits. Concluding, the development of a numerical model demands a lot of engineering judgment and experience in order to balance the restraints and the desirable outcome.

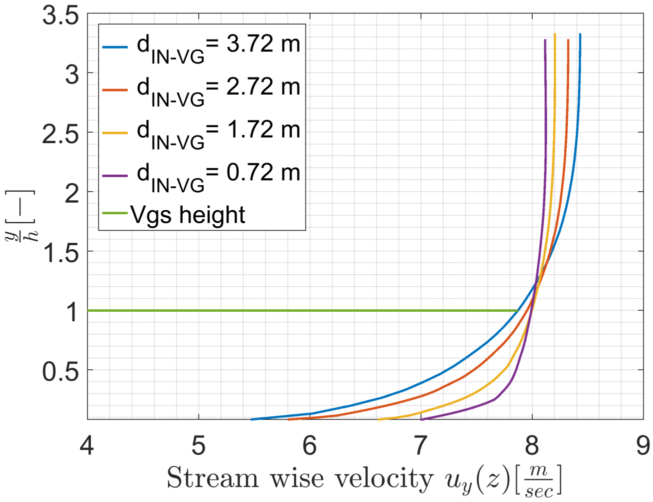

Figure 3.9: Velocity profiles of the parametric study

4. Results

In this part of the thesis, the results obtained from the numerical modelling are presented and compared qualitatively with the experimental ones in order to examine the behavior of the flow behind the VGs. The three velocity components (u_x,u_y,u_z) [$\frac{m}{sec}$] are extracted in the downstream plane sections by applying the isosurface function provided by the software. Figure 4.1 depicts the velocity field of the streamwise component in a plane section placed 3h downstream of the VGs while four symmetrical vortices are observed. The resultant velocity field of the figure below corresponds to the TrD configuration solved for the RST turbulence model. Two hundred isosurfaces are used for the general extraction procedure but Figure 4.1 includes only twenty isosurface lines in order to provide a satisfying visual result. At this point, it is important to note that only the results of the middle pair vanes will be presented for the ReD, since it yielded the most accurate results. The reason is that the mesh quality is significantly coarser for the outer vanes leading to more uncertain results (see Figure 3.6).

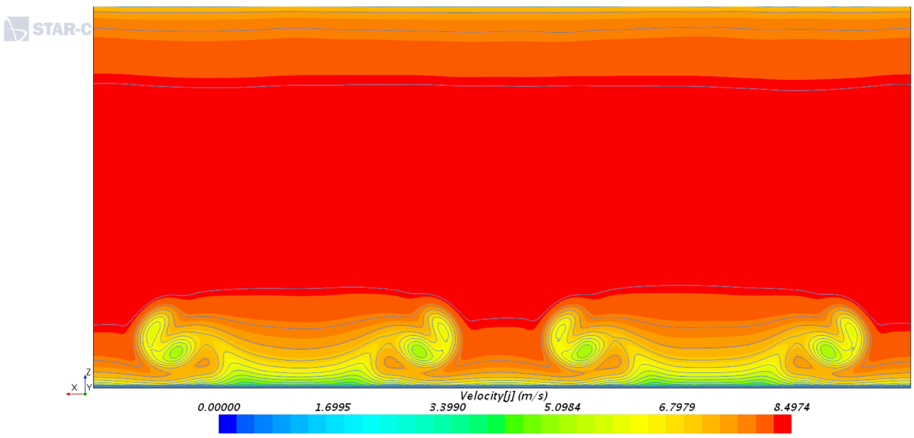

Figure 4.1: Isosurface lines implemented for the extraction procedure of the velocity values

For achieving a detailed comparison between the experimental and the numerical results, all the calculations are performed in Matlab using DTU's personal computer. It must be mentioned that the coordinate system used for the calculations is the experimental one defined below and for the rest of this chapter this is the only one used.

- x-axis: Streamwise direction
- y-axis: Vertical direction
- z-axis: Lateral direction

The model that is provided in order to compare qualitatively the experimental and numerical velocity fields is the RST turbulence model. For the ReD, the three velocity components are presented only at a plane 3h downstream of the VGs while the streamwise velocity is illustrated for all planes. For the TrD configuration, the resultant velocity fields in three directions are similarly provided up to the first investigated plane while the streamwise velocities are analyzed also for the 12h downstream plane. The color range is identical for both numerical and measured velocity fields.

4.1. Vortices generated from the rectangular devices

Figure 4.2 illustrates the numerical and the experimental streamwise velocity components in a section plane at 3h i.e 0.18 m downstream. In order to produce the velocity field, a mesh-grid for the ZY plane is created [-0.2:0.001:0.2, 0:0.001:0.2] [m] specifying the boundaries of the z and y axes. However the results presented in Figures below are normalized with respect to the VGs height,h i.e $\frac{z}{h}$,$\frac{y}{h}$.

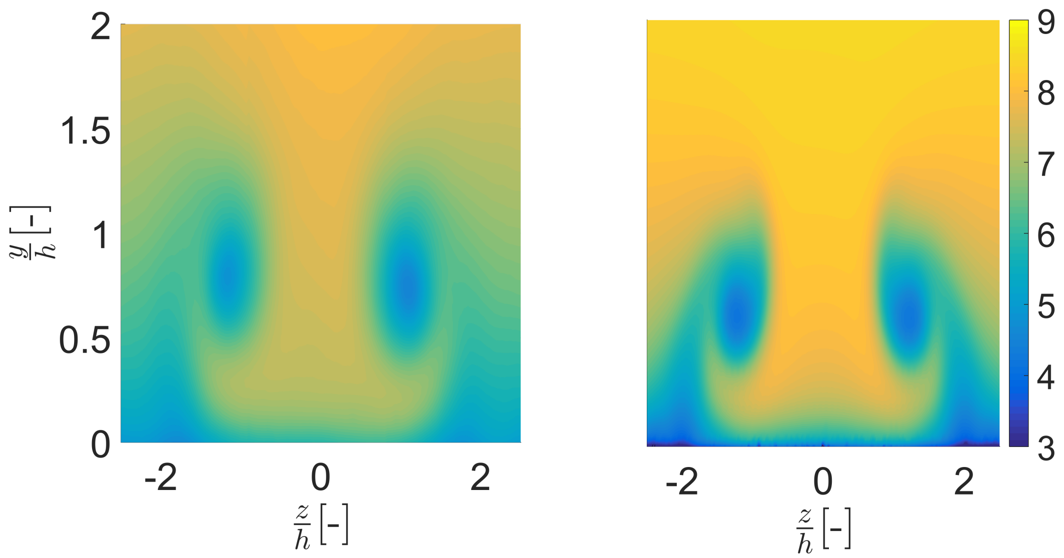

Figure 4.2: Comparison between the experimental (left) and computational (right) streamwise velocity components (x-direction) 3h downstream of the VGs

It is observed that the streamwise vortices develop downstream of the middle VG pair and induce momentum mixing from the free stream and near the wall region. A fine comparison between the experimental (right) and the numerical (left) streamwise velocity fields is depicted in the area close to the developing vortices. In the free stream region, the numerical model results in a streamwise velocity distribution with a lower gradation compared to the experiment. This indicates that the numerical model produces more 'distinct' vortices compared to the experimental while the latter seem to be more influenced by the high turbulent background. Specifically, this difference is may be a concern of meandering and the spatial averaging taking place in the measurements as C M Velte states in [1].

A similar procedure is followed in the y and z velocity components for experimental and numerical velocity fields.

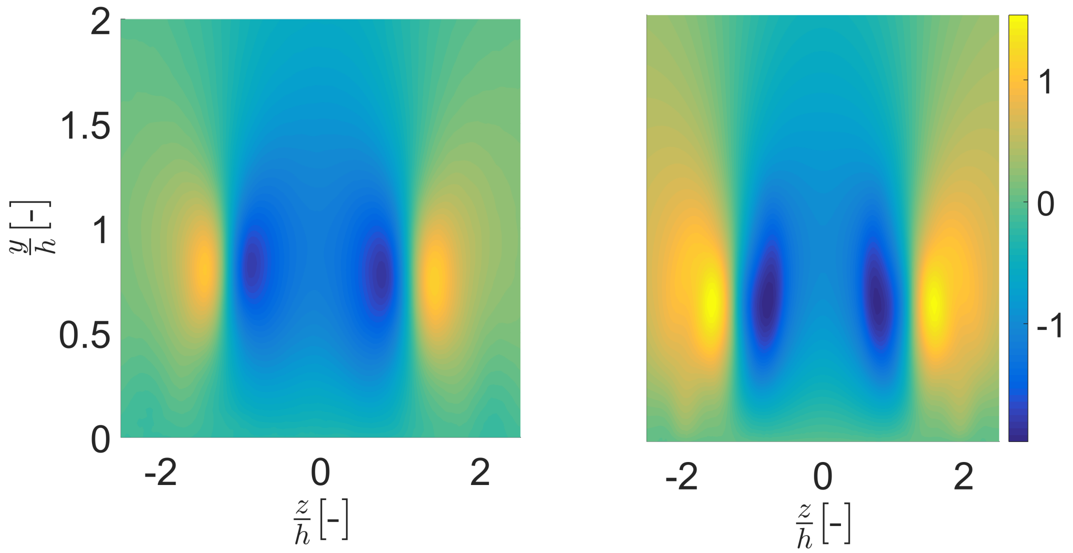

Figure 4.3: Comparison between the experimental (left) and computational (right) vertical velocity components (y-direction) 3h downstream of the VGs

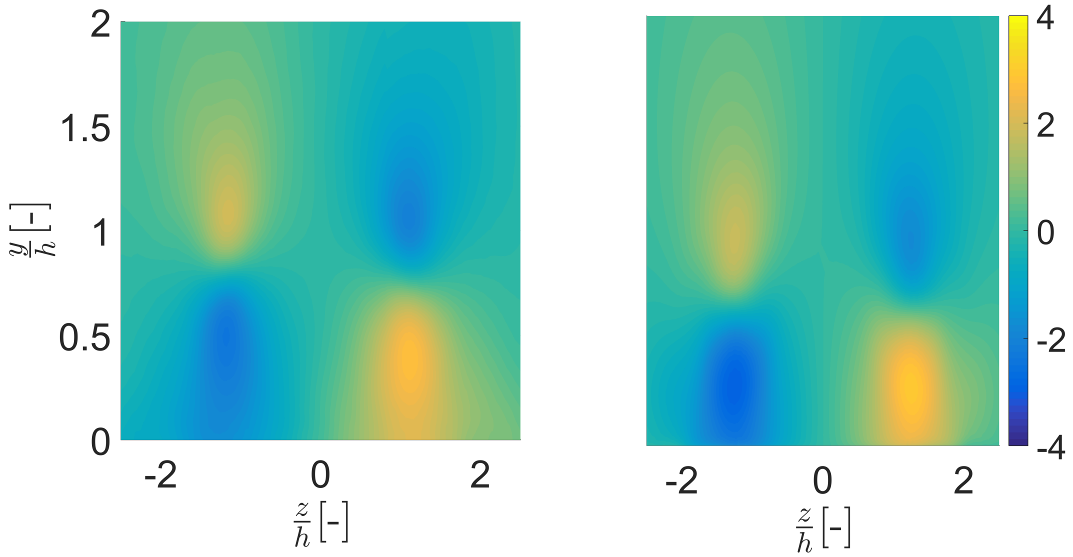

Figure 4.4: Comparison between the experimental (left) and computational (right) lateral velocity components (z-direction) 3h downstream of the VGs

Figure 4.4 shows that the z velocity components of the left and the right middle-pair vanes are point symmetric, while the y velocity components (Figure 4.3) are symmetric with respect to the y-axis. Thus, it can be derived that the vortices of the two vanes behave as counter-rotating vortices. In this case, the low momentum i.e momentum close to the wall is transported upward while the high momentum i.e momentum within the free stream region is transported downward.

The exact same procedure is applied in the further downstream planes. The velocity fields for the streamwise component (x-direction) are presented in Figures 4.5-4.8 while the y and z components can be found in Appendix B (see Figures B.1-B.8).

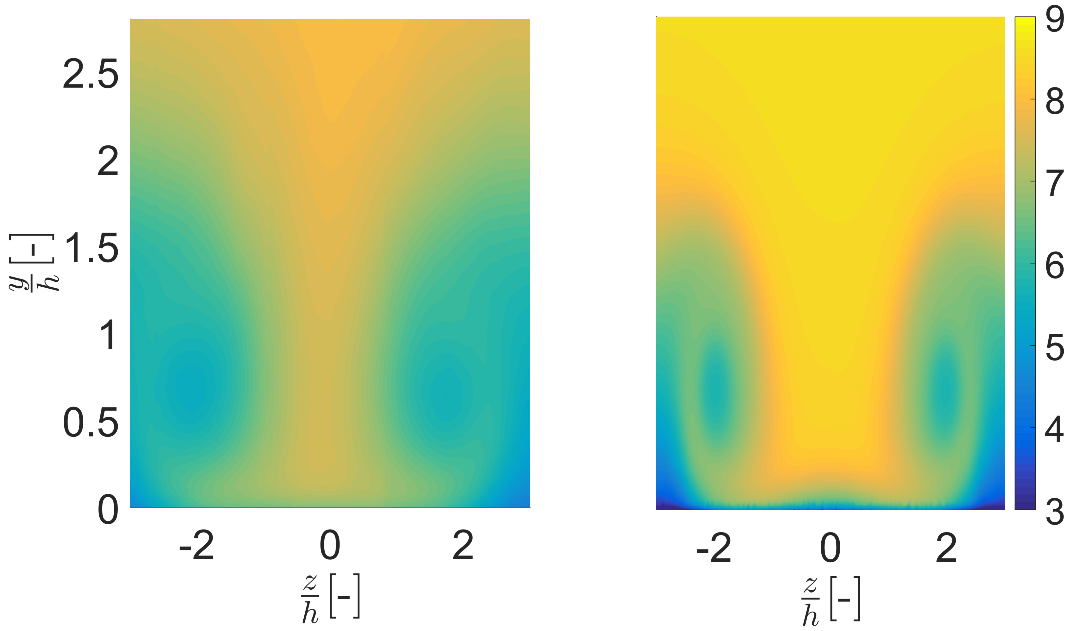

Figure 4.5: Comparison between the experimental (left) and computational (right) streamwise velocity components (x-direction) 12h downstream of the VGs

The normalized z-axis for the last three experimental velocity fields (Figures 4.6-4.8) is [-5:5] [-].

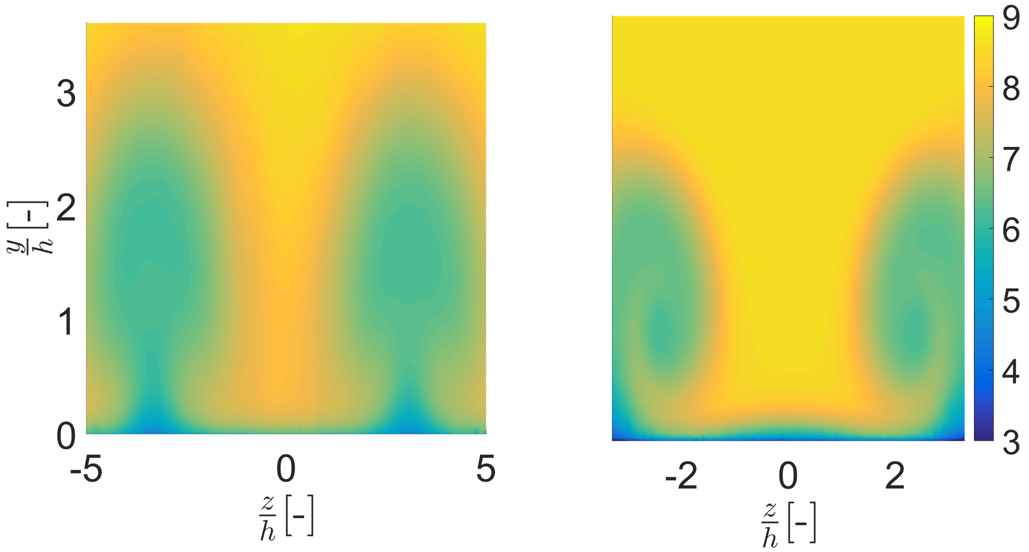

Figure 4.6: Comparison between the experimental (left) and computational (right) streamwise velocity components (x-direction) 25h downstream of the VGs

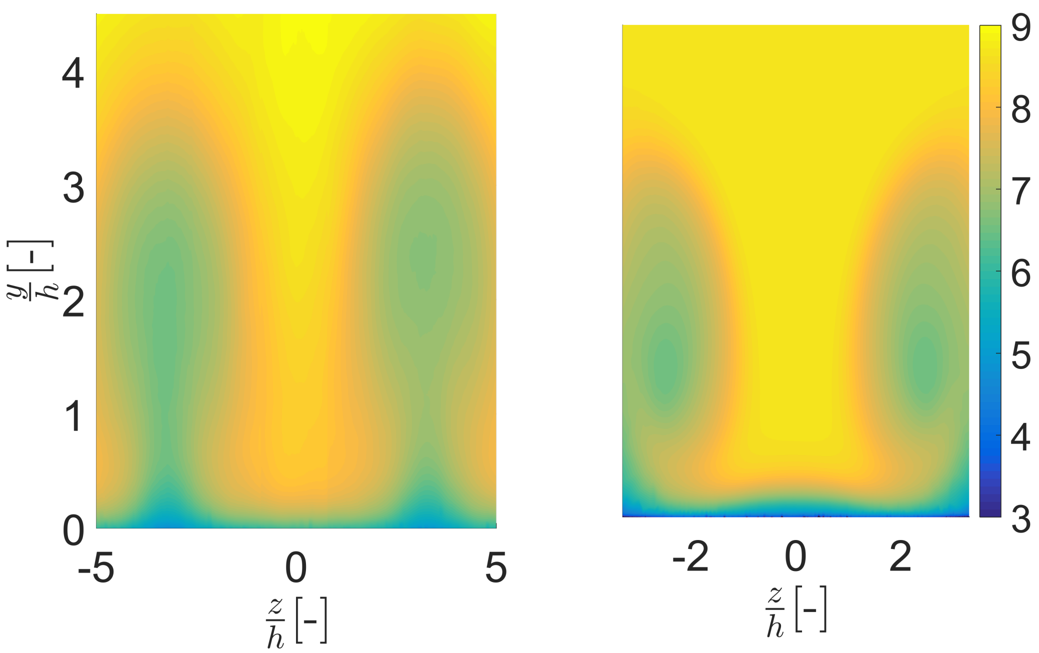

Figure 4.7: Comparison between the experimental (left) and computational (right) streamwise velocity components (x-direction) 40h downstream of the VGs

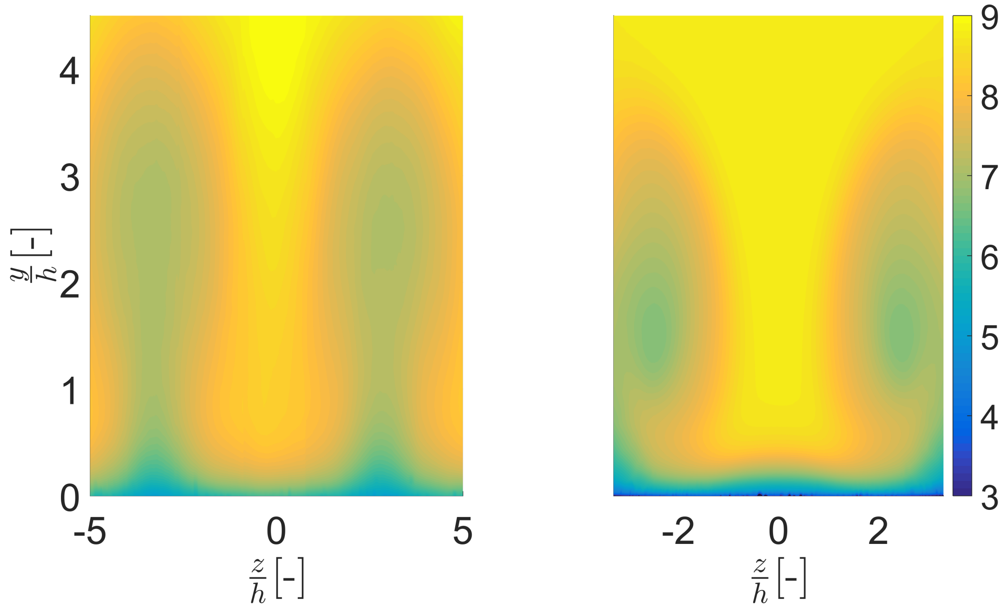

Figure 4.8: Comparison between the experimental (left) and computational (right) streamwise velocity components (x-direction) 50h downstream of the VGs

As the vortex propagate further downstream into the wake, the area that it covers increases and the streamwise velocity magnitudes within this area also increase. This phenomenon is more intense in the experimental data while the numerical vortices seem to be more confined. Therefore, it can be claimed that the resultant numerical vortices expand less into the wake than the vortices obtained from the experiment.

The shape of the vortex changes significantly and this can be observed after the 12h downstream (Figure 4.5). Especially in the experimental velocity fields, the circular area that the vortex covers becomes more oblique while the numerical vortices maintain a more circular shape with a growing radius into the wake. This alternation could be mainly caused by the merging of the vortices induced by the outer vanes with the ones induced by the middle-pair vanes. Even though the shape of the numerical vortex does not change significantly, this merging also occurs without being so clear since the mesh discretization is quite coarser out of the z-axis range [-3:3]. Although the coordinates of the vortex center are not defined yet, it can be seen that the vortex core moves in both lateral and vertical directions. More specifically, the motion of the core indicates that the vortex moves upwards in the vertical direction and slightly in the negative lateral direction in the 12h downstream plane. This variation is more intense in the rest of the downstream planes.

In general, the numerical model produces more distinct vortices in all investigated downstream planes. As aforementioned, one explanation for this regime is that the experimental data is a spatially averaged field consisting of thousand instant snapshots. One of these snapshots at 3h downstream can be seen in Figure 4.9.

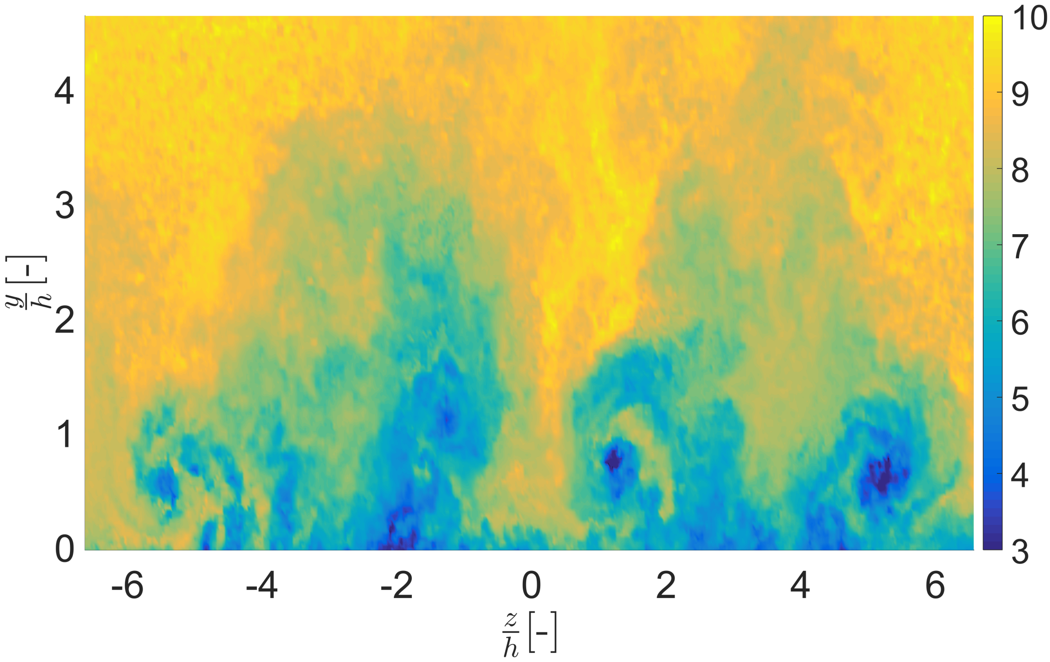

Figure 4.9: PIV snapshot at 3h downstream

This translates that the high turbulence background influences the investigated area while the RANS model cannot capture in detail these fluctuations since it averages all scales. Finally, the difference between the experimental shown in [1] and numerical incoming velocity profiles contribute in the discrepancies of the compared results.

4.2. Vortices generated from the triangular devices

A similar comparison between the velocity fields is also applied on the triangular configuration. In contrast to the ReD, the induced vortices of all the four vanes are presented since the quality of the mesh is uniform along the lateral range [-6:6]. The streamwise velocity is depicted in Figure 4.10.

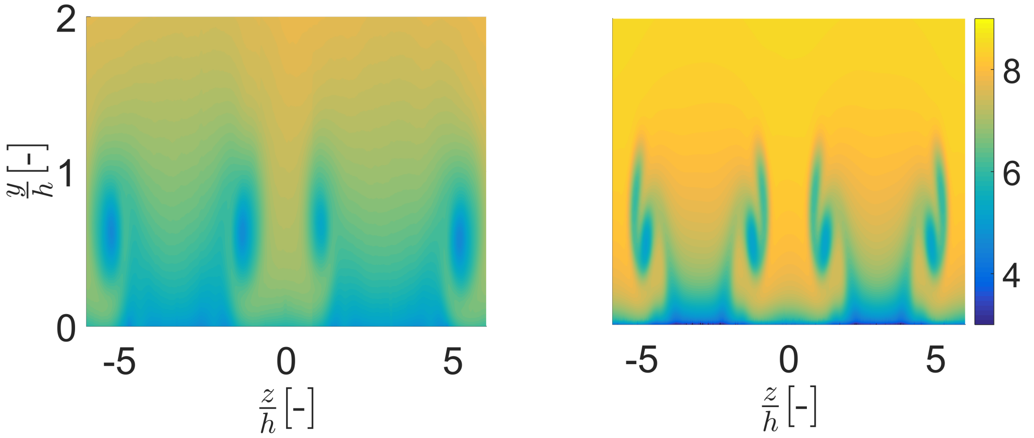

Figure 4.10: Comparison between the experimental (left) and computational (right) streamwise velocity components (x-direction) 3h downstream of the VGs (TrD)

The vertical,y-direction, and lateral,z-direction, velocity components are presented in Figures 4.11 and 4.12 respectively.

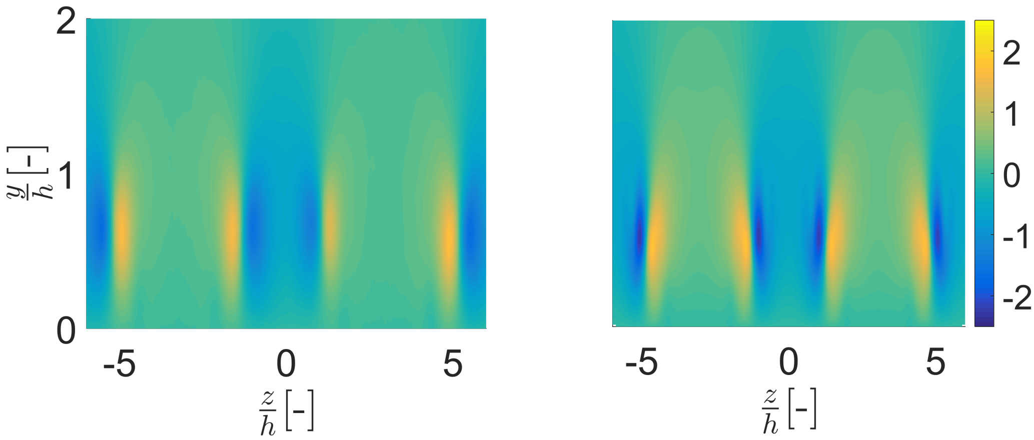

Figure 4.11: Comparison between the experimental (left) and computational (right) vertical velocity components (y-direction) 3h downstream of the VGs (TrD)

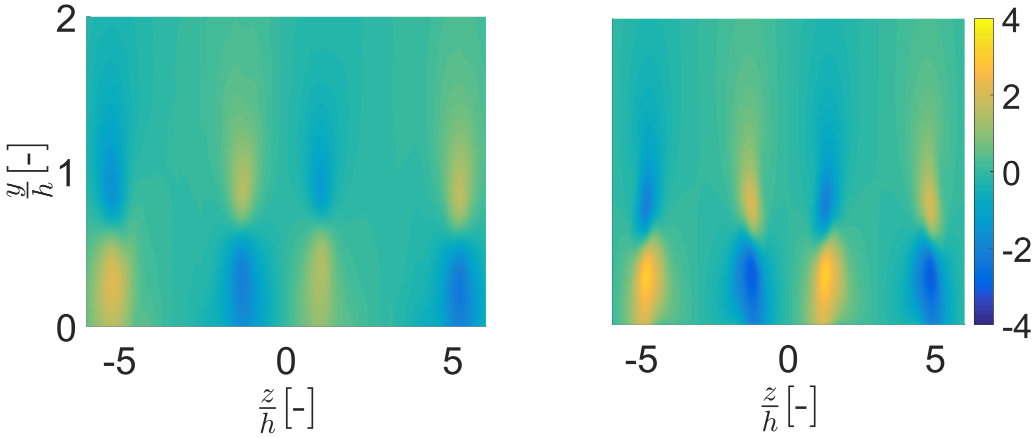

Figure 4.12: Comparison between the experimental (left) and computational (right) lateral velocity components (z-direction) 3h downstream of the VGs (TrD)

The velocity fields developed by the triangular vanes reveal a difference in the shape of the vortices compared to the ones induced by the rectangular configuration. Especially in the numerical streamwise velocity field at 3h downstream (Figure 4.10), more oval shaped vortices are developed in comparison to the circular shape derived by the ReD case. The different vortex formation can also be determined by the y and z velocity components (Figures 4.11 and 4.12). Focusing on the numerical results, the rectangular configuration where the momentum transfer is symmetrical to the vertical (Figure 4.11,right) and the lateral direction (Figure 4.12,right) i.e circular motion, the sideways motion (Figures 4.11 and Figure 4.12,right) contributes to the different formation of the vortex. However, this difference is not clearly seen in the experimental case.

Further downstream at 12h, the streamwise velocity components are shown in Figure 4.13.

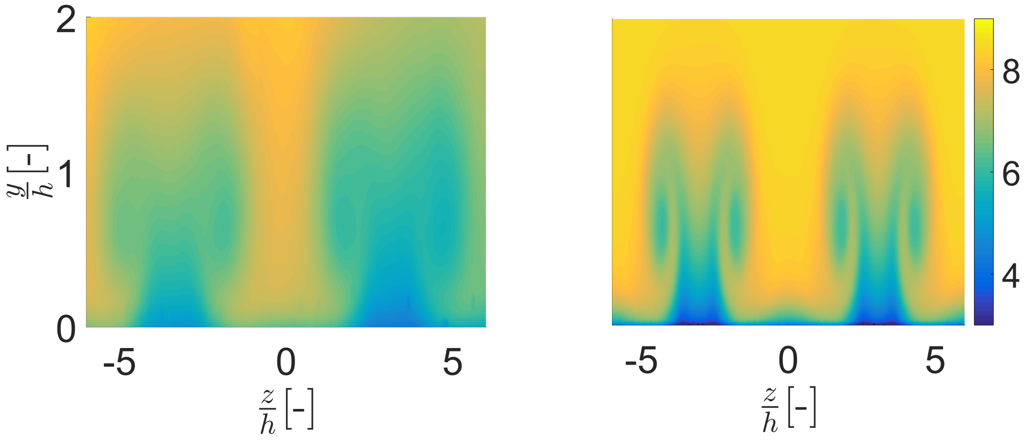

Figure 4.13: Comparison between the experimental (left) and computational (right) streamwise velocity components (x-direction) 12h downstream of the VGs (TrD)

Even though a solid comparison cannot be achieved due to the high turbulence in the experimental velocity field, it can be mentioned that the vortices tend to have similar shape with the ones derived by the rectangular configuration in Figure 4.2. The shape of the vortices is more circular than the oval shape of the 3h downstream plane and this can also be verified by the y and z velocity components shown in Appendix B (see Figures B.9 and B.10).

4.3. Investigation of streamlines

To examine thoroughly the contribution of the rectangular and triangular devices in the development of the vortices, 80 streamlines are extracted from the software. Streamlines by definition are a family of curves that are instantaneously tangent to the velocity vector of the flow. They show the direction in which a mass-less element will travel at any point in the fluid domain[2]. In Figure 4.14, the streamlines start from the upstream region within the high-pressure side of the middle-right vane.

Figure 4.14: Streamlines for the ReD (left) and TrD (right) configurations

As it is observed in the rectangular case (Figure 4.14, left), the downstream vortex is formed by the streamlines curling up along the tip of the vane. Starting from the leading edge, most of the streamlines follow a similar pattern resulting in a clear formation in the wake. The geometry of this formation could be characterized as a cylinder acquiring its shape right behind the vane. Close to the trailing edge, the streamlines define a similar swirling path which is assimilated to the main structure further downstream. On the other hand, the triangular vane (Figure 4.14, right) utilizes the whole hypotenuse side in order to generate the vortex. In this case, the trajectories vary depending on the point they collide with the hypotenuse side. This results in a vortex with a more irregular shape as the streamwise velocity component of Figure 4.10 depicts. Therefore, the impact of the investigated geometry on the vortex shape can be explained with the visualization of the streamlines.

Finally, it should be mentioned that the resultant velocity fields of the Spalart-Allmaras and k-ω SST turbulence models are not presented in this chapter since they display insignificant qualitative differences with the RST turbulence model. However, their contributions on the analysis of the flow behind the VGs are provided in the following chapter.

5. Validation

In this part, the results for the numerical model are further analyzed and compared quantitatively to the experimental results. The main indicator for the validation procedure between the numerical and the experimental results is the circulation of the velocity field. The estimation of the circulation is conducted with the direct use of the definition as well as with the use of the Lamb-Oseen Vortex. The analysis for estimating the circulation is presented for the 3h downstream plane for the RST turbulence model. However, the integral values of all three turbulence models in all downstream planes are presented in the end of this chapter. The circulation results are normalized i.e $\frac{\Gamma}{Uh}$ [-]

5.1. Determination of circulation with direct use of definition

Circulation is normally denoted Γ and it estimates the amount of fluid rotation within a closed curve C [2]. It could be stated that Γ contributes also at quantifying the actual strength of the vortex.

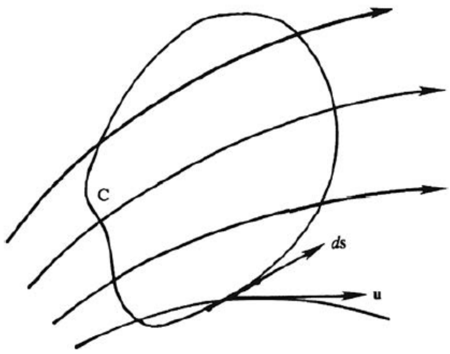

Figure 5.1: The amount of fluid rotation in a closed curve C [2]

By definition, Γ is the line integral of the dot product of the velocity u and the spatial element ds.

$$\Gamma = \oint_C u \cdot ds \tag{5.1}$$

In this research, the closed curve C was decided to be a circle of radius r with a center at the location of the center of the vortex. The location of the vortex center is determined as the fluid element with the minimum streamwise velocity u_x. The radius r is estimated taking into account two fundamental constraints:

- The circulation, Γ, of a vortex filament is constant along its length in order to fulfill Helmholtz's first theorem [23]. Thus, a different radius is defined for the vortices of each one of the downstream planes since the size of the vortex changes with respect to the downstream position as described in 4.1. For instance, if a small radius is applied in a far downstream plane e.g 40h, may not capture the fluid adequately.

- To estimate accurately the circulation of a vortex, the velocity vectors which intersect with the circle C must not be influenced by the neighboring vortex.

Thus, an empirical relation for the parametric study of the radius can be derived and can be seen in eq.5.2:

$$\begin{aligned} r_{num} &= C \cdot dz_{num} \\ r_{exp} &= \frac{C}{2} \cdot dz_{exp} \end{aligned} \tag{5.2}$$

where C is the parameter that varies, and dz_{num}=$1 \cdot 10^{-3}$ m , dz_{exp}=$2 \cdot 10^{-3}$ m are the grid steps for the numerical and experimental fields respectively. In order to fulfill the two constraints, C for the first downstream plane is decided to be equal to 25 resulting in a r equal to $2.5{\cdot}10^{-2}$ m. The z,y coordinates of the velocities are defined from the circle definition. For instance, the numerical locus of points are estimated from eq. 5.3.

$$\begin{aligned} z_{num} &= r_{num} \cdot \cos(\theta) \\ y_{num} &= r_{num} \cdot \sin(\theta) \end{aligned} \tag{5.3}$$

where θ =$[0 : \frac{\pi}{720} : 2\pi]$

In Figure 5.2, the two counter rotating vortices of the numerical vector field can now be presented as well as the circle for the line integration with the predefined center and a radius r. A zoomed-in plot of the velocity field of Figure 5.2 can be found in Appendix C (see Figure C.1) for a more detailed visualization.

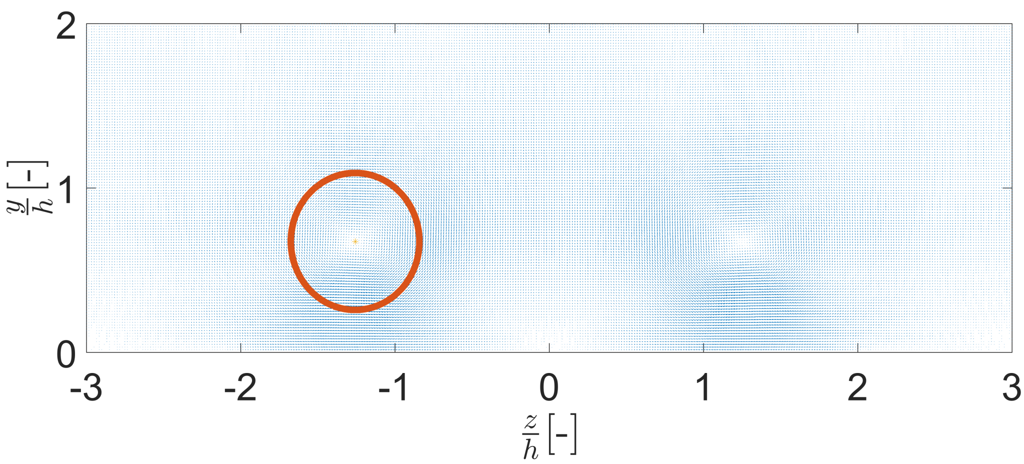

Figure 5.2: Field of the numerical velocity vectors $u(u_z, u_y)$ in the corresponding coordinates (z,y)

In order to complete the calculation of Γ integral, velocity u needs to be specified. The red circle of Figure 5.2 defines the boundaries where the lateral and the vertical components of velocity field u(u_z,u_y) are extracted. Figure 5.3 includes the decomposed velocity components u_z and u_y attached to that circle for both numerical and experimental velocity fields.

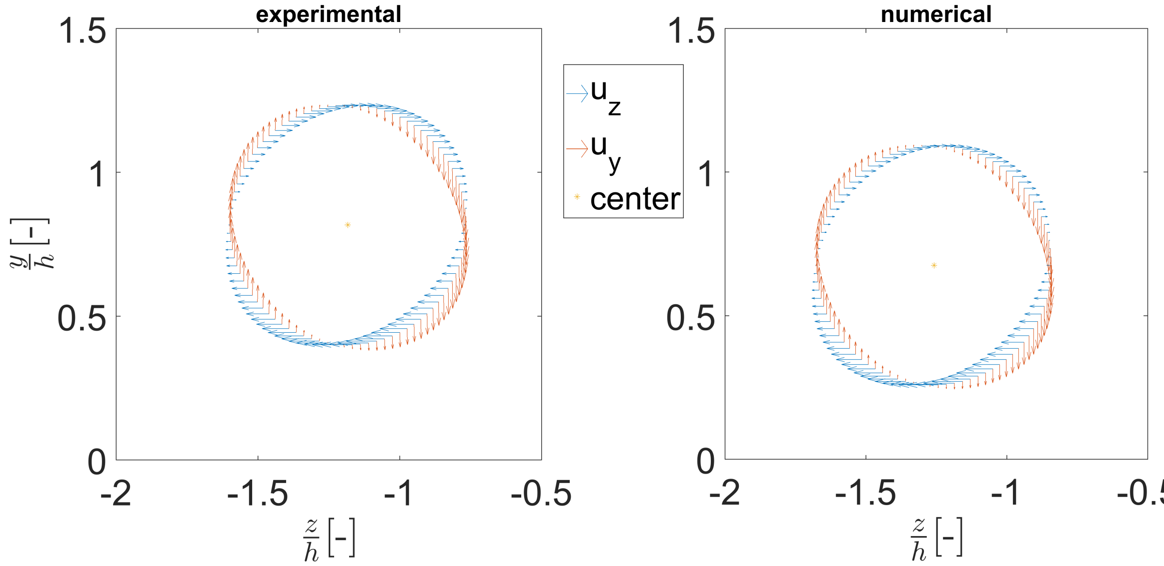

Figure 5.3: Experimental (left) and numerical (right) velocity components u_z and u_y of velocity vectors u(u_z, u_y) (ReD)

The center of the experimental vortex core depicted in Figure 5.3 is [-1.182,0.817] while for the numerical is calculated equal to [-1.258,0.6758].

All Γ integrations are transformed from the Cartesian to the polar coordinate system using eq. 5.4 and a schematic representation of the radial and tangential velocity components can be found in Appendix C (see Figure C.2). The variation of the tangential velocities u_θ along the predefined circle will also indicate on how well the experimental velocities fit with the numerical values.

$$\begin{aligned} u_r &= u_z \cos\theta + u_y \sin\theta \\ u_\theta &= -u_z \sin\theta + u_y \cos\theta \end{aligned} \tag{5.4}$$

Assuming that the tangential velocity u_θ of eq.5.4 remains constant within a small angular segment, the definition of eq. 5.1 can be numerically evaluated in the polar form using Matlab by implementing the summation of eq. 5.5.

$$\Gamma = \sum_{i=1}^{n} u_{\theta_i} r \Delta\theta_i \tag{5.5}$$

where $\Delta\theta$ is the angular segment equal to $\frac{\pi}{720}$ and n is equal to $\frac{2\pi}{\Delta\theta}$ i.e 1440 angular segments. Therefore, the numerical integration derives the following four magnitudes for the experimental and numerical circulation which are presented in table 5.1.

Table 5.1: Circulation estimated with use of definition at 3h downstream using the RST turbulence model

Geometry	Γ_{exp}	Γ_{num}
ReD	-0.621	-0.635
TrD	-0.535	-0.567

Apparently, the values are negative since the middle-left vortex rotates to the negative x-direction as shown in Figure 5.2. It is clear that the numerical and experimental Γ results are quite similar for the ReD while the difference is slightly higher for the TrD. Even though the integral values are close, the comparison of the implemented tangential velocities indicate that differences exist.

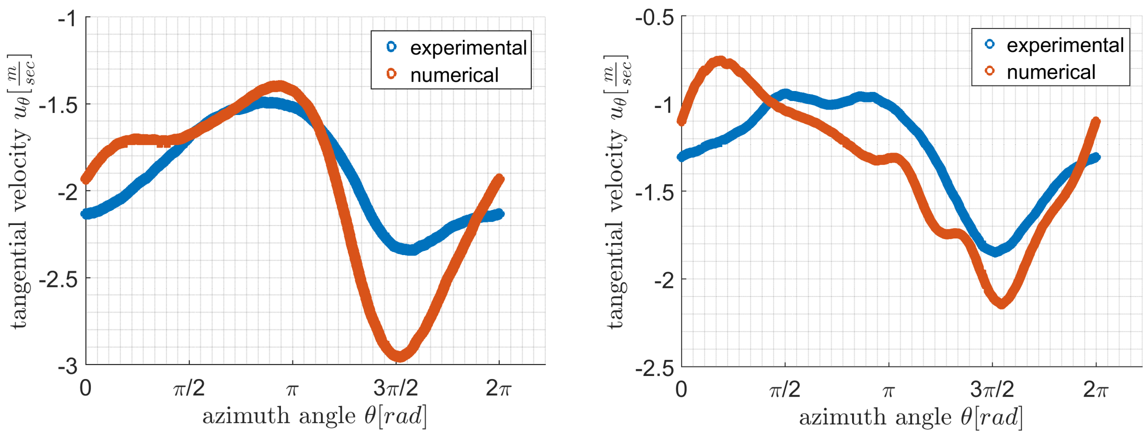

Figure 5.4: Azimuth variation of tangential velocities of the ReD (left) and TrD (right) at 3h downstream for the RST model for ReD and TrD

At first, it should be stated that the azimuthal variation follows an anti-clockwise pattern:

- Close to the free stream region: $\frac{\pi}{2}$
- Close to the walls: $\frac{3\pi}{2}$

Starting from the ReD, it can be stated that the numerical tangential magnitudes are higher close to the walls (area around $\frac{3\pi}{2}$), while in the rest of the investigated region a fine agreement between the experimental and the numerical results can be observed. Both, numerical and experimental velocities follow a sinusoidal pattern without a constant amplitude. This behavior can also be verified by the lateral velocity components of Figure 4.4 which are identical to the tangential components at $\frac{3\pi}{2}$ and $\frac{\pi}{2}$.

In the TrD case, the numerical tangential velocities are slightly higher compared to the experimental but both present a quite analogous behavior. A clear peak also appears close to the walls in the lateral direction.

As shown in the previous chapter, differences exist between the actual topologies of the numerical and the experimental vortices and these differences can also be verified by the quantitative analysis for both experimental and numerical results. However, the estimation of Γ indicates that the two vortices have almost the same strength and the force that exert on the surrounding fluid particles is approximately the same.

5.2. Determination of circulation using Lamb-Oseen Vortex

To validate the accuracy of Γ calculations deriving from the integral definition, the Lamb-Oseen Vortex (LOV) is implemented. This model introduces an analytical solution on the Navier-Stokes equations [24]. It states that if a vortex filament exists, with some strength equal to Γ, the velocity field in a distance r can be derived by eq. 5.6.

$$u_z(y) = \sum_{1}^{n} \frac{-(y_p - y_v) \cdot \Gamma}{2\pi r^2} \cdot (1 - e^{(-(\frac{r}{r_\epsilon})^2)})\ [\frac{m}{sec}] \tag{5.6}$$

where (z_v, y_v) corresponds to the location of the vortex center and (z_p, y_p) are the points where the induced velocities (u_z, u_y) are estimated. The radius r used in this relation is equal to $\sqrt{(z_p - z_v)^2 + (y_p - y_v)^2}$ and r_ϵ [m] is the vortex core radius.

In order to estimate the circulation with the use of the above described equation, the procedure described bellow needs to be followed:

- At first, the velocity profiles $u_z(y)$ for both numerical and experimental results are extracted along a line that crosses the vortex location center and it is vertical to the streamwise direction i.e y-direction.
- The $u_z(y)$ velocity profile of eq.5.6 is estimated in the same coordinates with an initial guess in Γ value. So, z_p remains constant while y_p varies n times (upper limit of sum Σ in eq.5.6).
- The vortex core radius r_ϵ that is used corresponds to the numerical core radius and it is equal to $\frac{y|_{u_z(y)=max} - y|_{u_z(y)=min}}{2}$. It can also be defined as the radius where the tangential velocity u_θ is maximum [25].
- A parametric analysis in Γ value of eq.5.6 is conducted in order to fit the numerical velocity profiles with the velocity profile of eq. 5.6.

The outcome of this procedure for the 3h downstream plane using RST turbulence model is presented in Figure 5.5.

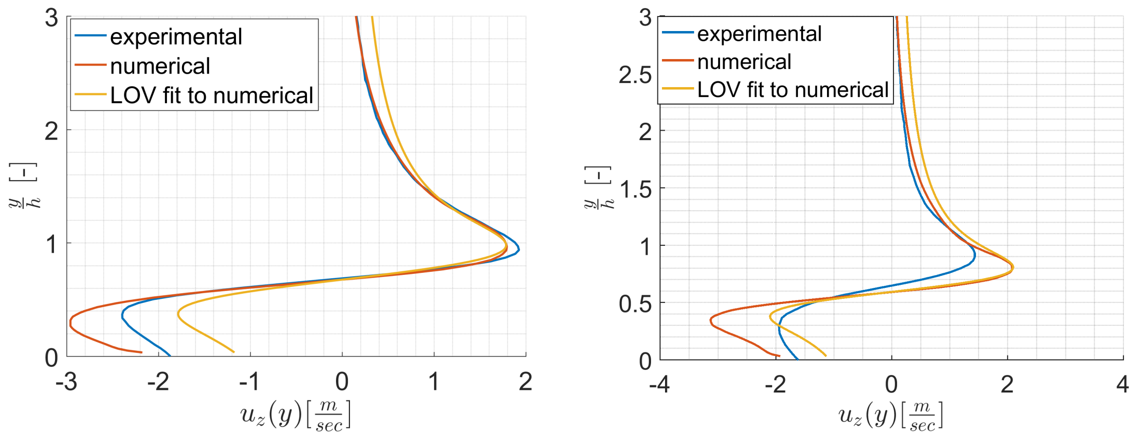

Figure 5.5: Determination of Γ with the use of Lamb-Oseen Vortex for the ReD (left) and TrD (right) at 3h downstream

In the ReD configuration, the Γ value that is used in order to build the velocity profile of Figure 5.5 (left) is equal to -0.6 which is quite similar to the values presented in Table 5.1. The vortex core radius is equal to 0.035 corresponding to the numerical core radius. As it is expected, the LOV produces an axisymmetric behavior since it assumes cylindrical symmetry [24]. On the other hand, the experimental and the numerical velocity profiles present higher $u_z(y)$ magnitudes close to the walls compared to the region near the free stream. For this reason, an improved fitting between the numerical velocity profile and the one derived from LOV cannot be achieved. This non-symmetrical behavior of the experimental and numerical vortices can also be verified from the azimuthal distribution of the tangential velocities in Figure 5.4.

In the TrD case (Figure 5.5,right), the Γ value used for the creation of the LOV profile is equal to -0.55 . The non symmetrical behavior of the numerical and experimental velocity profiles can also be observed.

Figure 5.5 also provides useful information on how accurately the numerical model simulates the experiment. In the ReD, it can be concluded that the lateral $u_z(y)$ velocity profiles are identical apart from the area close to the wall where the numerical models results in slightly higher velocity magnitudes. On the other hand, the TrD profiles shows that the numerical model produces higher velocity values along the vertical direction. In the measured data, only the rectangular devices provide a clear distinction of the vortex cores from the turbulent background [1]. This indicates that the comparison of the lateral velocity profiles of the TrD may include uncertainties. However, the overall comparison of the above two velocity profiles indicates that the numerical model can actually approach the realistic behavior of the flow really close to the VGs i.e 3h downstream.

5.3. Circulation results

So far, the determination of the circulation is analyzed in the first downstream plane i.e 3h, for one turbulence model. Therefore, it is required to follow the same procedure in all investigated planes, for the three turbulence models and the two geometries in order to evaluate the computations further into the wake. Figures 5.6-5.8 illustrate the comparison between the experimental and numerical circulation estimated with the direct use of definition and the circulation results obtained from the Lamb-Oseen Vortex in all downstream planes. The circulation results are presented in absolute values.

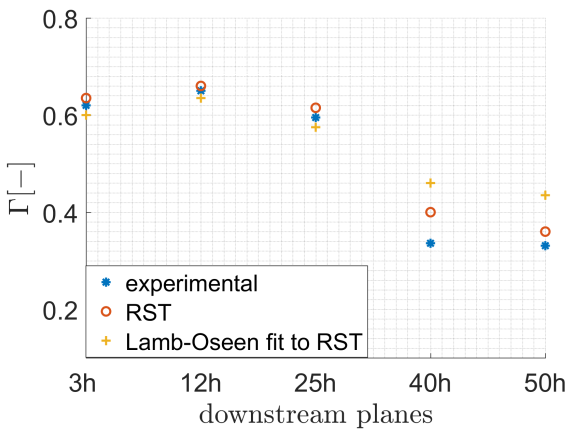

Figure 5.6: Numerical circulation calculated with the direct use of definition and Lamb-Oseen Vortex compared to experimental circulation (RST turbulence model for the ReD)

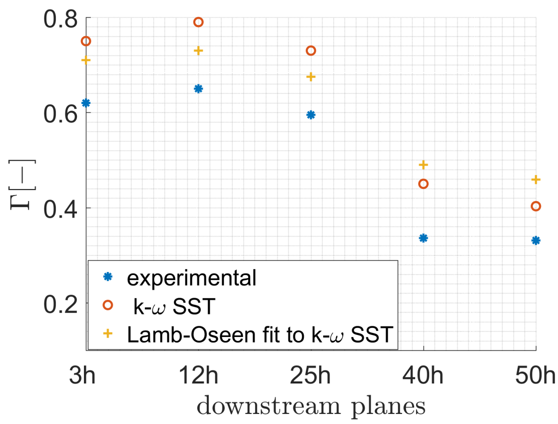

Figure 5.7: Numerical circulation calculated with the direct use of definition and Lamb-Oseen Vortex compared to experimental circulation (k-ω SST turbulence model for the ReD)

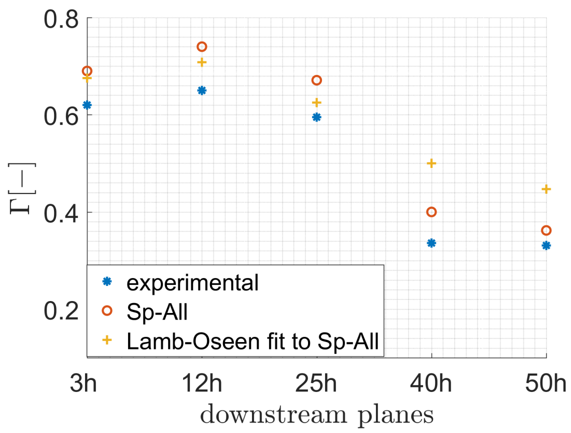

Figure 5.8: Numerical circulation calculated with the direct use of definition and Lamb-Oseen Vortex compared to experimental circulation (Spalart-Allmaras turbulence model for the ReD)

Starting from the ReD configuration and the RST turbulence model, all circulation results are approximately 0.6 (in absolute values) for the first three downstream planes. As the vortex develops further into the wake, the circulation slightly decreases. In real fluids, the dissipation of the vortex due to viscosity contributes in the observed drop.

Computational issues may also exist in the calculation of the circulation. Specifically, it is expected that the circulation estimated by the LOV is lower than the corresponding estimated by the definition since the latter results always in lower velocity magnitudes compared to the numerical $u_z(y)$ velocity profile, due to its axisymmetric behavior (see Figure 5.5). However, this relation between the circulation deriving from the path integration and the one deriving from LOV does not exist in the last two downstream planes even if the corresponding fit is quite analogous (Appendix B,see Figure C.3) to the one illustrated in Figure 5.5. Therefore, it can be stated that the circulation deriving from definition may be underestimated in the last two investigated planes while the LOV circulation produces higher circulation results.

One explanation for this miscalculation using the line integral may be the mesh discretization of the fluid domain in these plane sections. As explained in 4.1, the mesh grid is coarser out of the z-range [-3:3]. In the ReD configuration, the boundaries of the integrated circle slightly exceed this range. This difference in the quality of the mesh may produces improper velocity magnitudes leading to an unreliable path integration only for the last two downstream planes.

The k-ω and Spallart-Almaras turbulence models result in a discrepancy between the numerical and the experimental Γ values for the first three downstream planes while the circulation decreases in the rest of the investigated planes similar to the RST turbulence model.

In the experimental case, the circulation follows quite a similar pattern and this can be also validated up to the 25h downstream plane. Since the boundary layer is highly turbulent and the instantaneous vortex cores are not always well distinguishable as C M Velte states in [1], the estimation of the experimental circulation also includes uncertainties. For instance, the Lamb-Oseen Vortex cannot provide an accurate fitting to the experimental velocity profile in the last two downstream planes. This is mainly caused by averaging in the velocity fields. The z-coordinate where the lateral measured velocity is maximum cannot be estimated accurately. The discrepancy between the numerical and the experimental estimations in the last two downstream planes can be seen in Figure 5.6.

Accordingly, the Γ values for the TrD configuration in the two downstream planes are provided in Figures 5.9-5.11.

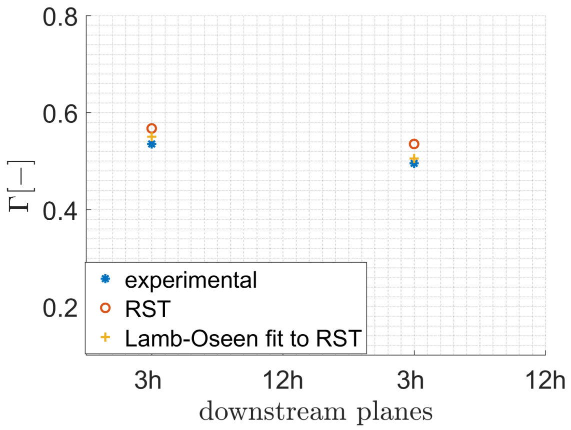

Figure 5.9: Numerical circulation calculated with the direct use of definition and Lamb-Oseen Vortex compared to experimental circulation (RST turbulence model for the TrD)

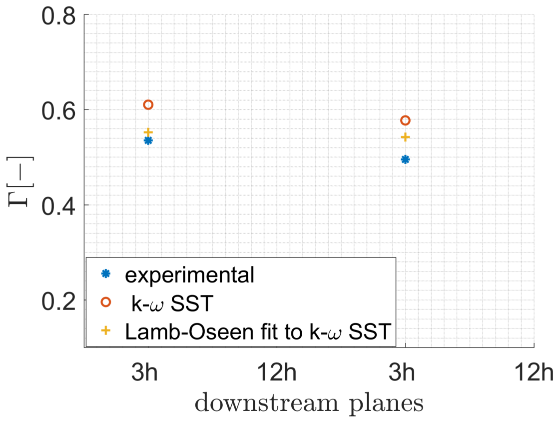

Figure 5.10: Numerical circulation calculated with the direct use of definition and Lamb-Oseen Vortex compared to experimental circulation (k-ω SST turbulence model for the TrD)

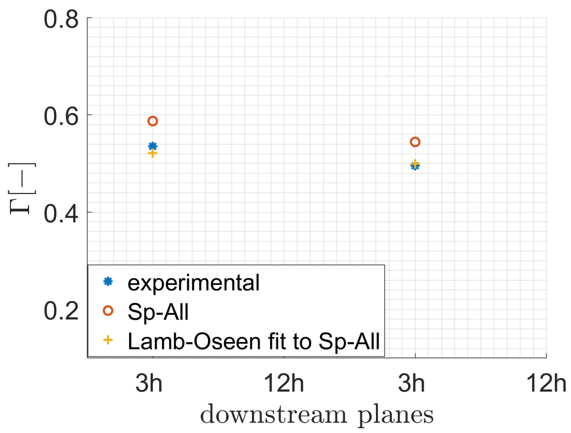

Figure 5.11: Numerical circulation calculated with the direct use of definition and Lamb-Oseen Vortex compared to experimental circulation (Spalart-Allmaras turbulence model for the TrD)

In 4.2, it is shown that the formation of the induced vortices is highly correlated with the two investigated geometries. However, the circulation of the vortices from the TrD is almost the same with ReD case as Figure 5.9 depicts. As shown in the previous chapter, both numerical and experimental circulation are quite similar with the use of the RST turbulence model. For the second investigated plane i.e 12h the circulation slightly decrease. As in the ReD case, both k-ω SST Spalart-Allmaras turbulence models seem to derive a higher circulation compared to the RST turbulence model and to a higher discrepancy compared to the experimental results.

The evolution of the vortex in the wake is also characterized by the vortex core diameter ϵ. As aforementioned the vortex core diameter is defined as the distance between the locations where the maximum and minimum lateral velocities exist: $\epsilon = y|_{u_z(y)=max} - y|_{u_z(y)=min}$. Figures 5.12 and 5.13 illustrate the growing of the vortex core diameter as the vortex develops downstream.

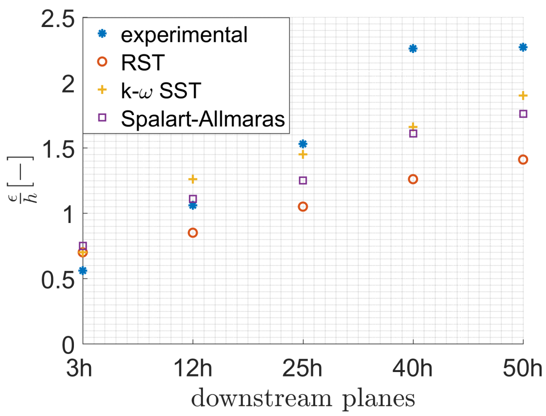

Figure 5.12: Vortex core diameter ϵ [-] for the ReD configuration

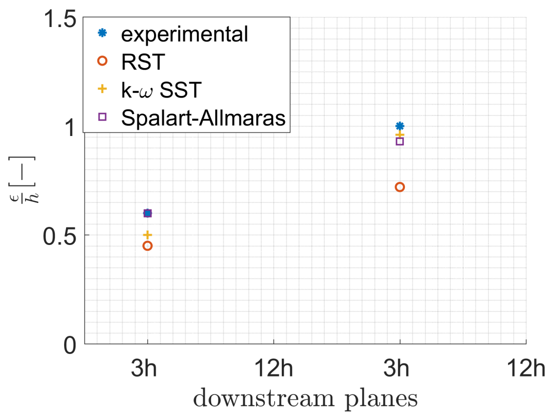

Figure 5.13: Vortex core diameter ϵ [-] for the TrD configuration

As it is expected, the vortex core diameter increases as the vortex moves into the wake for all turbulence models and experimental results. For the ReD configuration, the RST turbulence model induces more confined vortices i.e shorter diameter compared to the Spalart-Allmaras and k-ω turbulence models in all downstream planes. Specifically, in the first downstream plane and for the RST turbulence model, the vortex has a diameter almost equal to $\frac{1}{2}$h and quite similar to the experimental one, while in the most downstream position it is slightly larger than h and the corresponding experimental equal to almost 2h. This difference between the experimental and the numerical diameters in the last two investigated planes may be enhanced by the high turbulent regime that mentioned by Velte et al [1]. As mentioned, the experimental vortex cores are not well distinguishable due to the high turbulent boundary layer. Thus, the estimation of the vortex core diameter is uncertain in the last two downstream planes.

6. Hypothesis for the VGs

In this part of the report, the lifting line theory for wings of finite span is investigated for the VGs case. This theory derives a correlation between the trailing and the bound vortex. In order to test if this theory is valid for the VGs case, the circulation results in the wake obtained from definition and LOV are compared with the one obtained from this hypothesis. The successful results of this hypothesis were also presented in WESC 2017 and the presentation can be found in Appendix E.

Trailing vortex is the one formed downstream of the VG similar to the induced vortex which is examined in the previous chapter. Bound vortex is the one that represents the physical structure of the VG and its strength i.e circulation is variable. Specifically, the bound vortex is strongest near the mid-span i.e mid-height in VGs case, and weakest near the tip [5]. Helmholtz's theorem states that a vortex filament cannot begin or end in a fluid; it must end at a wall or form a closed loop [5]. Thus, as the bound vortex weakens from the mid-height to the tip, it releases vortex filaments parallel to the streamwise direction. These vortex filaments originated from the spanwise gradient of the bound vortex are supposed to curl up in order to form the trailing vortex. For the evaluation of this theory, it is assumed that the summation of the circulation of these vortex filaments is equal to the trailed circulation. In the aircraft's wing case where this theory is widely used, it is assumed that the aspect ratio i.e span/averaged chord is so large that the problem can be treated as a 2D problem. Thus, it is crucial to test if the VGs behave as conventional wings where the aspect ratio is significantly low. A definition for the aspect ratio for both devices can be found in Appendix D (see Figure D.1)

Assuming that the VG behave as a wing, the bound circulation at its location is estimated with the use of the Kutta-Joukowski lift theorem from the 2-D airfoil theory [5]. This theorem derives a relation between the lift force and the bound circulation and it is presented in eq. 6.1 below.

$$l(z) = \rho \cdot u_y(z) \cdot \Gamma(z) \; [\frac{N}{m}] \tag{6.1}$$

In this investigation, the air density ρ(P,T) is equal to 1.1812 $\frac{kg}{m^3}$ and $u_y(z)$ is the streamwise velocity at each height z. Even though the experimental coordinate system is established for the results and validation chapters, it is decided to use the orientation of the numerical model in order to provide helpful images extracted from the software.
The coordinate system used for the numerical simulations is:

- x-direction: lateral direction
- y-direction: streamwise direction
- z-direction: vertical direction

The coordinate system can also be seen in the rectangular configuration in Figure 6.1.

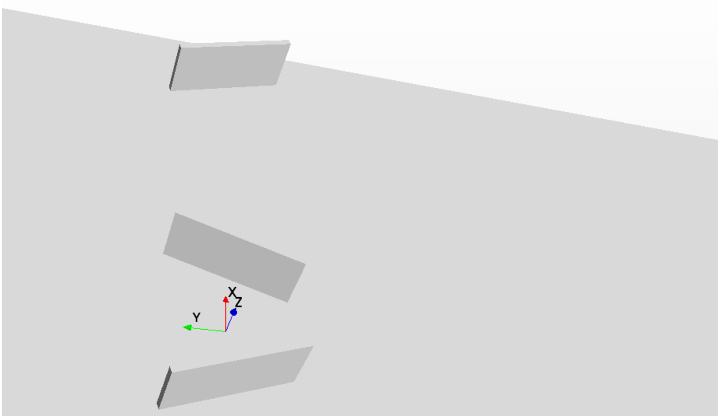

Figure 6.1: Coordinate system for the numerical simulations in STAR-CCM+

6.1. Analysis for the rectangular devices

Starting from the ReD case, the velocity at each location $u_z(y)$ of eq. 6.1 is extracted from the numerical simulations and the corresponding profile is shown in Figure 6.2. The probe line which correspond to the velocity values is placed $3h$ upstream of the VGs.

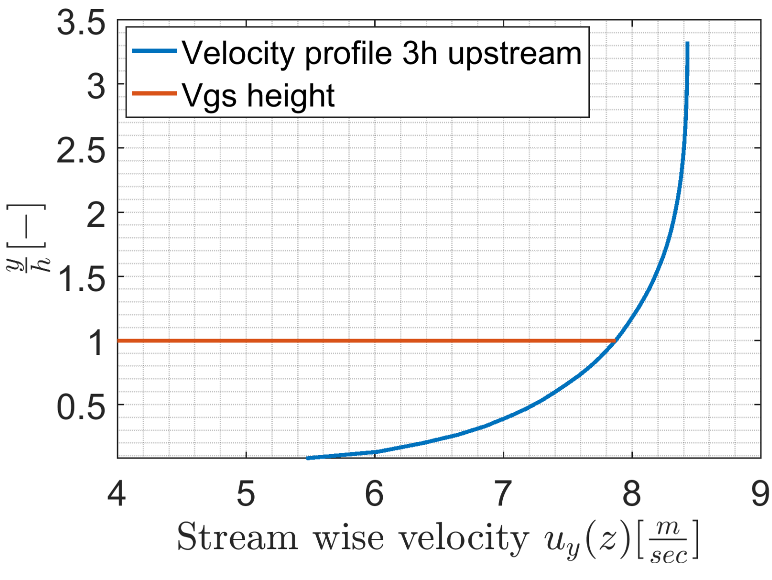

Figure 6.2: Extracted velocity profile $u_z(y)$

Since the velocity at each height is known, the lift force can now be calculated. A fundamental way to achieve that is to project the pressure force normal to the incoming flow as eq 6.2 states.

$$l(z) = F(z) \cdot cos(\beta)\ [\frac{N}{m}] \tag{6.2}$$

The reacting pressure force F(z) from the flow, is analyzed into a direction perpendicular to the free stream velocity and to a parallel direction to U [5].

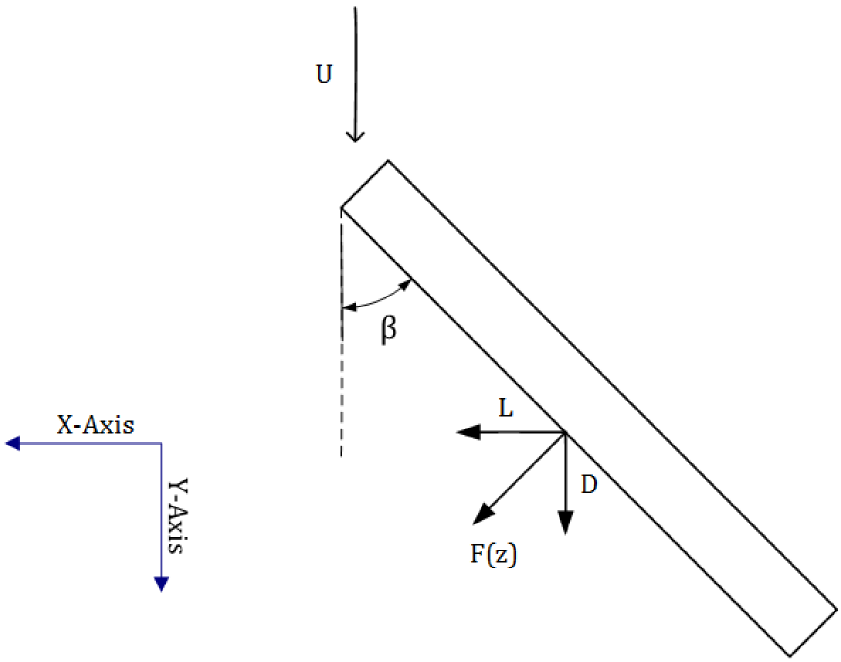

Figure 6.3: Lift and drag forces as projections of pressure force at a height z

where β is the VG angle and is defined as the angle between the VG and the streamwise direction of the flow. In this case, angle β is equal to 18°. Knowing the pressure jump at each height z, the net pressure force can be estimated by the following integral.

$$F(z) = \int_0^h \Delta P(y, z) dy\ [\frac{N}{m}] \tag{6.3}$$

where h is equal to 0.06 m. Figure 6.4 corresponds to a XY plane intersecting the VGs at $\frac{z}{h} = 0.5$ and illustrates the overall pressure field for the converged solution of RST turbulence model. It can be clearly seen that two pressure regions exist close to VG, one dominated by high pressure values and the other one by low pressure values.

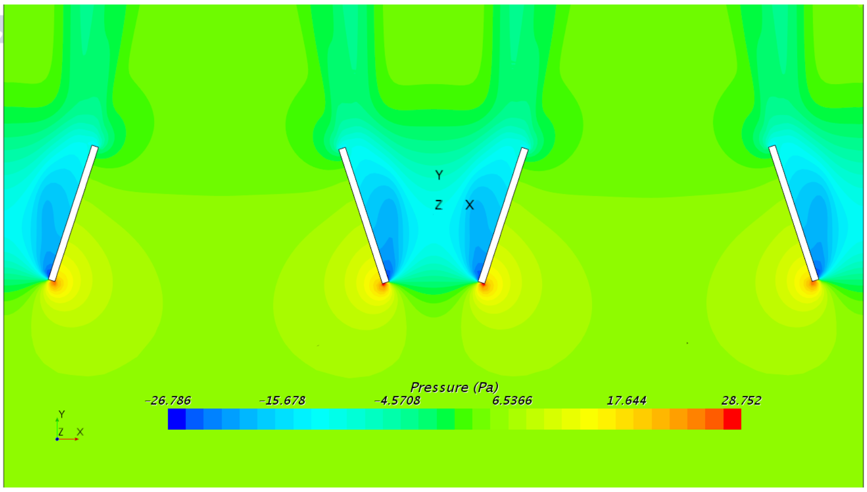

Figure 6.4: Pressure field in the XY plane, $\frac{z}{h} = 0.5[-]$

The pressure data are obtained in seventeen different heights with a step of $\frac{z}{h}$=0.056 by applying the built-in function line probe in STAR-CCM+. It is decided to avoid obtaining pressure values really close to the floor e.g $\frac{z}{h}$ 0.05 since an abnormal pressure behavior is observed. Figure 6.5 shows these probe lines in a smaller sample of heights.

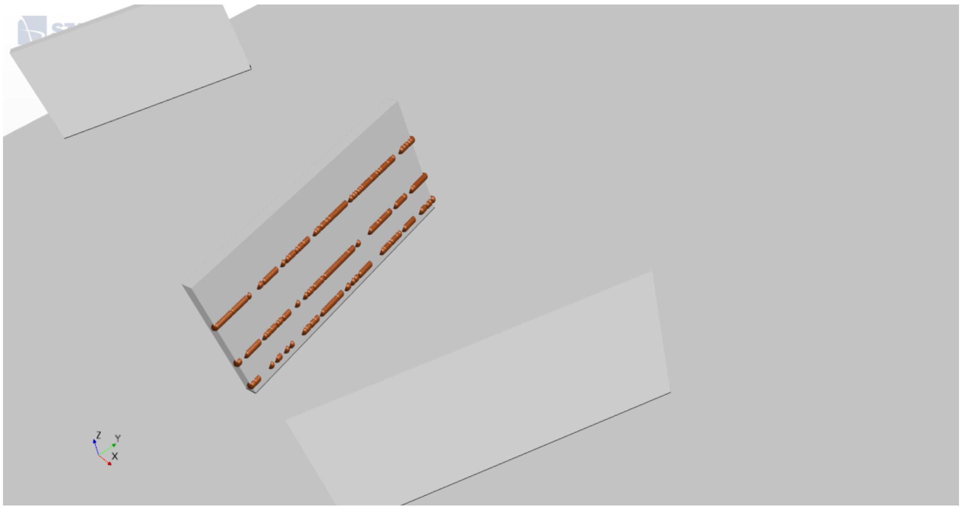

Figure 6.5: Extracted pressure values along the rectangular VG

Also, a sample of the pressure distributions $P_z(y)$ for both high and low pressure sides is presented in the following Figure 6.6.

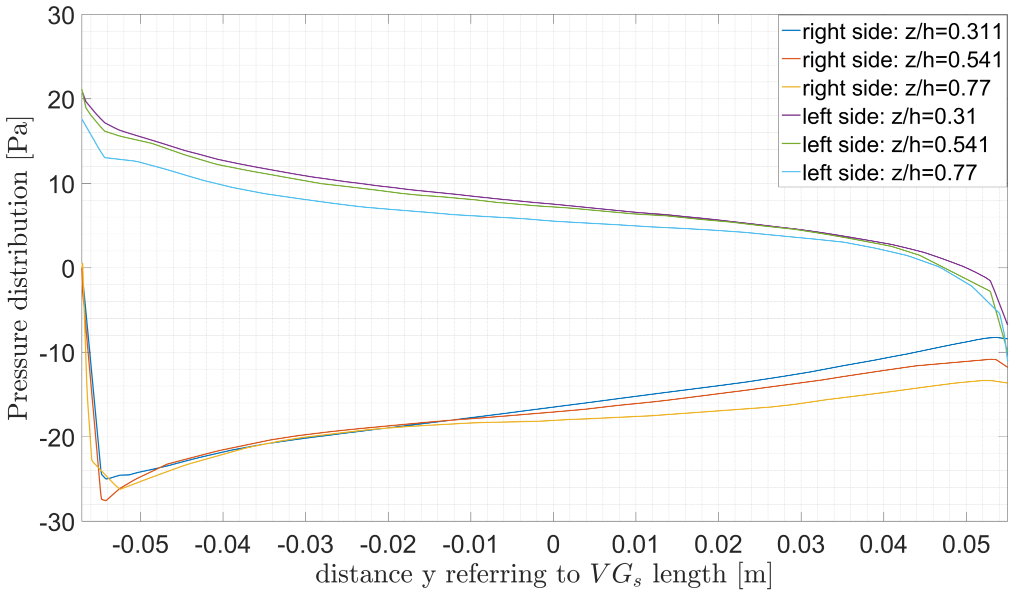

Figure 6.6: Pressure distribution on both sides of the VG

Since the lift is calculated at each height from eq.6.2 the bound circulation can now be estimated using the Kutta-Joukowski equation (eq.6.1). The distribution of the bound circulation along the VG height is shown in Figure 6.7.

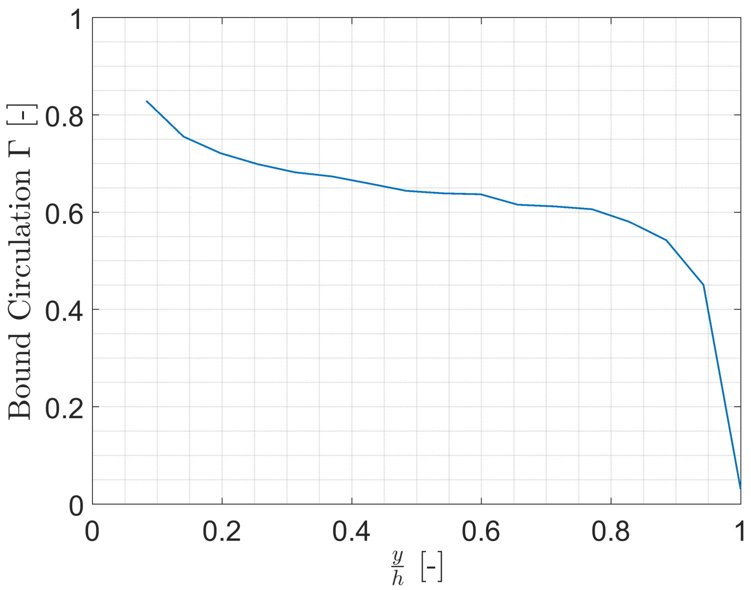

Figure 6.7: Distribution of bound circulation Γ for the rectangular VG

The distribution of the bound circulation follows a reasonable pattern since it weakens from the root to the tip of the VG height. However, the bound circulation presents slightly higher values close to the root than in the mid-height as the above described theory states.

As aforementioned, the released vortex filaments due to the weakening of the bound vortex turn parallel to the streamwise direction and roll up forming the tip vortices. The trailed circulation of this tip vortices, can be numerically evaluated in the intermediate heights j between the investigated heights i, $\Gamma_j = \Gamma(i+1) - \Gamma(i)$ as described in the introduction of this chapter.

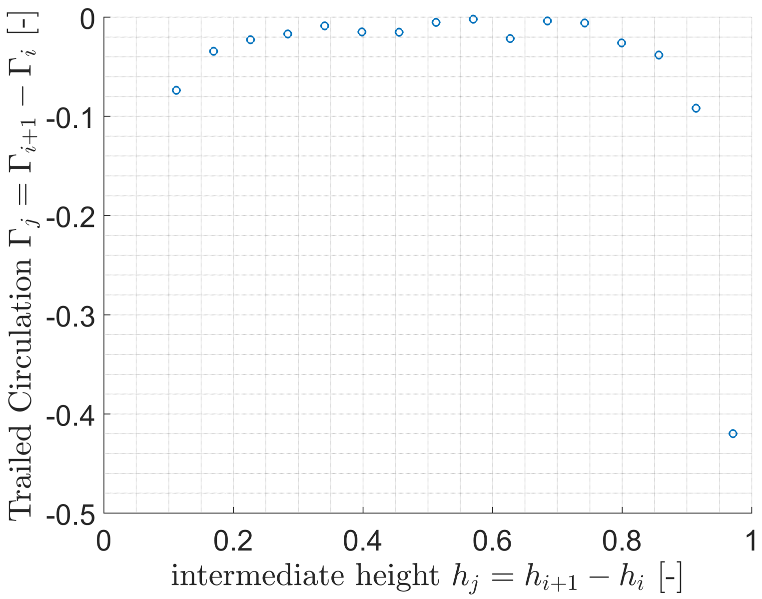

Figure 6.8: Trailed Circulation Γ for intermediate heights j on the rectangular VG

The trailed circulation Γ close to the tip is strongest than in the rest of the VG's height since the spanwise gradient $\frac{d\Gamma}{dz}$ is the largest. In a real flow case, the formation of the trailing vortex is not associated only with the strong tip vortex but the released trailing filaments also contribute on it [5]. Therefore, it can be assumed that the circulation generated by the vortex filaments between the mid-span and the tip results in the trailed circulation. The summation of the circulation of these filaments results in a Γ value equal to 0.597 in absolute value. This value is almost identical with the circulation calculated from the line integral definition and the LOV using the RST turbulence model in the previous chapter. Therefore, it can be stated that this hypothesis can be applied in the rectangular VGs within these flow specifications even if the aspect ratio is really low.

6.2. Analysis for the triangular devices

The same analysis is conducted in the TrD configuration in order to test if the triangular VGs also behave as conventional wings. The velocity profile is the same with the one used for the ReD analysis since the physical properties of the two investigated configurations are identical. Thus, the pressure data are the only information that need to be extracted from the software. The extraction procedure is conducted again with the use of the probe line function as depicted in Figure 6.9 .

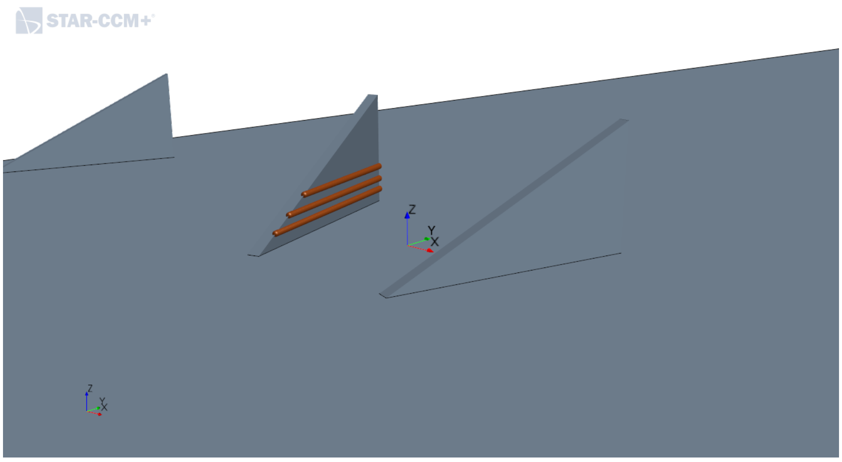

Figure 6.9: Extracted pressure values along the triangular VG

The extraction process in the TrD configuration is time consuming since the software does not provide the coordinates of the created geometry. Specifically, all the points on the hypotenuse side are specified manually through a visual inspection of the geometry. Similarly to the ReD, the pressure values are extracted in seventeen heights along the VGs height. The pressure distribution on both sides of the triangular VG are not presented as do in the ReD case (Figure 6.6) since the y-limits along the hypotenuse side change as a function of height z. The bound circulation on the triangular VG can be seen in Figure 6.10.

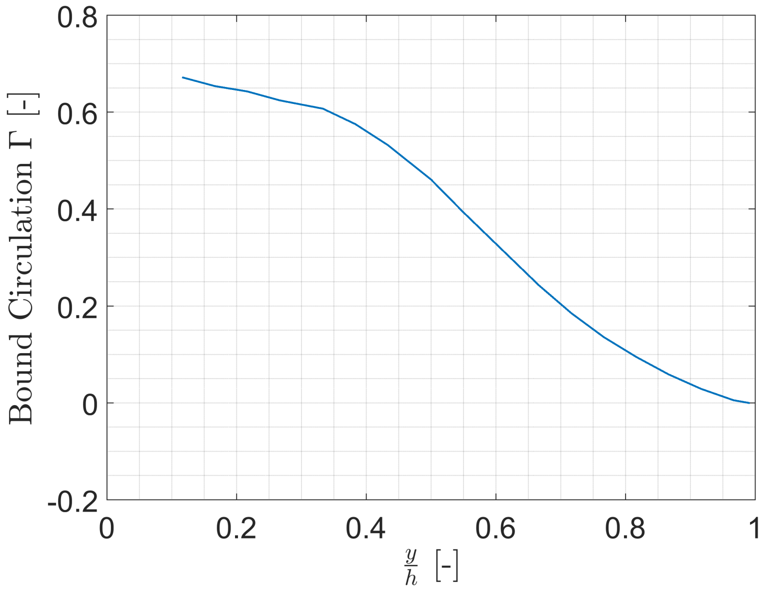

Figure 6.10: Distribution of bound circulation for the triangular VG

As it is expected, the bound vortex is stronger near the mid-height than the tip of the VG. However, the slope of the above curve is different compared to the one presented in Figure 6.7. In the ReD case (Figure 6.7), the bound circulation decreases with a really low gradient within a $\frac{y}{h}$ range [0.2:0.8], while in the tip the drop of the curve is significantly sharper compared to the rest of VGs height. On the other hand, the slope of the bound circulation in the triangular case can be divided in two regions. From the root to $\frac{y}{h}$ close to 0.6, the bound circulation is curved upwards i.e the slope decreases, while in the rest of the VG height the bound circulation is curved downwards i.e the slope increases. This behavior can also be verified by the trailed circulation which is illustrated in Figure 6.11.

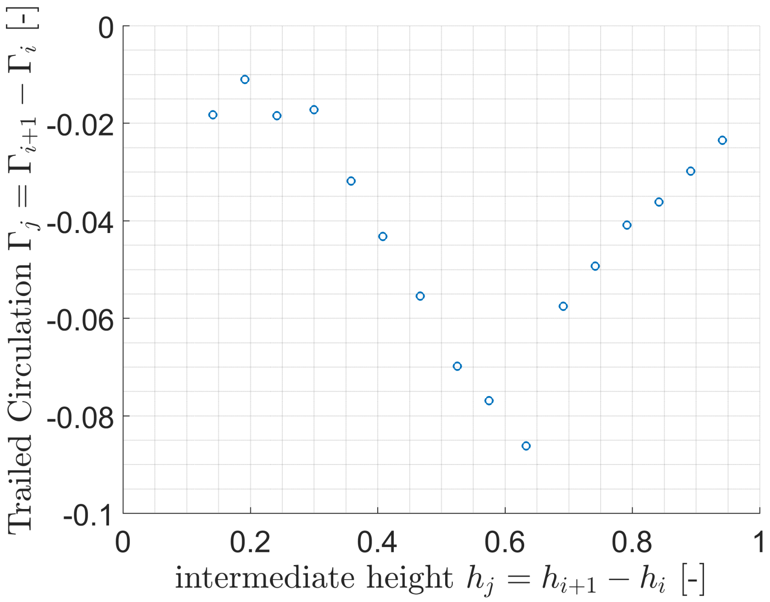

Figure 6.11: Trailed Circulation Γ for intermediate heights j on the triangular VG

The highest magnitude of the trailed circulation is observed on the inflection point where the slope of the bound circulation changes, while in the ReD case the strongest filament is the one released from the tip. Furthermore, most of the vortex filaments result in higher circulation compared to the previous case where the circulation included in most of the filaments was close to zero. Consequently, the behavior of the of the trailed circulation in the TrD case is quite different with one obtained from the ReD case. However, the summation of the circulation filaments from the mid-height to the tip is equal to $|-0.525|$. This value is close to the circulation obtained from the definition and the LOV which is approximately 0.56.

The difference that is observed between the trailed circulation formed by the rectangular VG (Figure 6.8) and the one formed by the triangular VG (Figure 6.11) could be associated with the streamlines which are investigated in 4.3 (Figure 4.14). As aforementioned, the triangular vane utilizes the whole hypotenuse side in order to generate the vortex. Therefore, the streamlines start to swirl from a low height close to the root until the tip of the VG. The rotating motion of these streamlines could indicate that the released vortex filaments have some actual strength i.e circulation. On the other hand, the rectangular vane make use only of the area close to the tip in order to create the trailing vortex. This could explain why the trailed circulation is stronger close to the tip than it is in the rest of the span.

7. Discussion

In this chapter, the findings of this research are further examined. The importance of the outcome is indicated and its practical application is introduced. At last, some ideas for future work are illustrated and approaches in order to enhance the numerical model are recommended.

RANS modelling

The analysis conducted in the previous chapters indicates that it is possible to resolve accurately the flow past the rectangular and triangular VGs operating in a turbulent boundary layer. However, issues still exist when the results of a RANS model are compared qualitatively with an experiment conducted in a realistic turbulent regime. One important issue is the meandering of the vortices that takes place in the experiment as Velte et al. state in [1]. Apart from the motion of the vortex center, this meandering may also be a result of the velocity fluctuations. It is visualized in Figure 7.1 where the location of the vortex location center of each PIV snapshot is presented. The vortex center is identified as the point with minimum axial velocity and maximum vorticity.

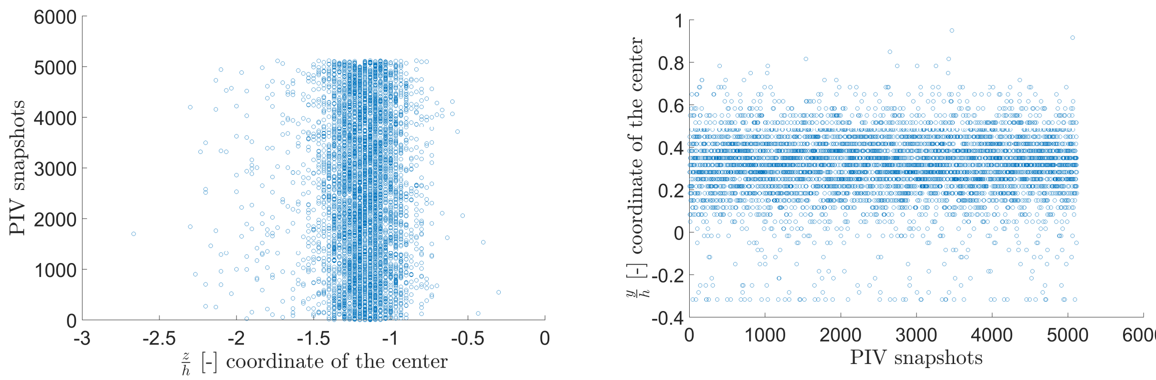

Figure 7.1: Meandering of the vortex center

In the PIV method, these vortex centers are spatially averaged in order to obtain the mean velocity field presented in 4.1 (Figure 4.2). This averaging leads to a turbulent qualitative outcome which is not sufficiently captured by the RANS model. As it is already known, RANS is based on averaging all scales and for this reason can only produce a time averaged mean value for the velocity field without monitoring the time dependent variations.

Estimation of circulation

The three Turbulence models that are implemented in order to close the RANS equations are the Reynolds-Stress, k-ω Shear Stress and the Spalart-Allmaras. In the quantitative part of the flow analysis the main parameter that is examined is the circulation with the direct use of integral definition and with the use of the Lamb-Oseen Vortex. It is demonstrated that the Reynolds-Stress Turbulence model provides more trustworthy results than the k-ω SST and the Spalart-Allmaras models. The Reynolds Stress Model represent the most complete classical turbulence model since it avoids the eddy viscosity approach and the individual components of the Reynolds-Stress tensor are directly computed. In most of the cases, the Reynolds-Stress model offers significantly better accuracy than eddy-viscosity based turbulence models [26]. However, the Reynolds-Stress model requires significantly more computational time for a converged solution compared to the other two models.

Implementing the Reynolds-Stress model, the numerical circulation determined with both the use of the definition and Lamb-Oseen Vortex agrees quite well the experimental circulation up to the third investigated plane which is placed 25h downstream of the rectangular configuration. In the last two investigated planes i.e 40h and 50h downstream, the circulation depicts a drop. This signifies that the dissipation due to viscosity may lead to that decrease or/and the direct use of the velocity integration includes uncertainties only in the last two investigated planes. For instance, the curve i.e circle, that is used in order to define the path for the line integration is probably influenced by the mesh quality regarding the numerical results and the meandering of the vortices regarding the experimental results. In the triangular configuration, the circulation is also calculated with path integration in two downstream planes and it is also validated with the use of the Lamb-Oseen Vortex. Even if the triangular vanes make use of half the area compared to the rectangular, the circulation results that they produce are close. Thus, it can be concluded that both rectangular and triangular configurations produce the same impact on the strength of the vortices with these flow specifications.

Benefits from the verification of the hypothesis for the VGs

One important outcome of this research is the hypothesis verified for the VGs case. In the latter chapter, the correlation between the bound and the trailed circulation was investigated and validated for the VGs, as on conventional wings. Even if the aspect ratio is low, the Kutta-Joukowski theorem from 2D airfoil theory is valid and the bound circulation of the vortex is actually associated with the lift force as for wings of a finite span. Assuming that the lift forces of a specific VG configuration are measured over a flat plate as on common airfoils, a good approximation of the circulation can be derived. Therefore, an important amount of time is saved since the analysis of the wake with the use of a numerical model is not required in order to estimate fairly the strength of the generated vortices.

Future work & Recommendations

- Improvement of mesh discretization: In the far wake, an improved mesh discretization is required in order to capture the development of the generated vortices in detail. Achieving an optimized mesh in the 40h and 50h downstream, the investigation of the flow and the line integration will be enhanced.
- Investigation of VGs width: In this research, the investigated width is set equal to 10 mm. A preliminary research revealed that the width does not cause significant differences in the circulation while it plays a dominant role at the mesh discretization and at the computational time. However, a numerical model with a shorter

downstream area and various investigated widths is required. This could provide important information about the pressure distribution on the pressure and suction sides of the VGs.

- Investigation of boundary conditions: In the last chapter, the investigation of the bound circulation seems reasonable apart from the area near the floor. Instead of using wall as a boundary condition, a symmetry plane condition will contribute on the determination of the circulation and the further investigation of this hypothesis.
- Implementation of field-functions: The software used for the numerical modelling does not provide the exact coordinates of the created geometry parts. Therefore, the coordinates of the extracted pressure data are determined by visual inspection. Especially in the TrD case, the identification of the points along the hypotenuse side include uncertainties. For this reason, a set of field functions is required in order to locate the points in detail.

8. Conclusion

In this thesis, two numerical models that fully resolve the rectangular and the triangular geometries of the VGs were built with the use of the commercial CFD software STAR-CCM+. The modelling is based on the experimental set up presented in [1]. The mesh discretization for the rectangular model consists of $11.3 \cdot 10^6$ cells while for the triangular model is approximately $8.2 \cdot 10^6$ cells. The three Transport Turbulence models used in order to close the RANS equations are: k-ω SST, Reynolds-Stress and Spalart-Allmaras.

The generated flow was investigated by comparing to PIV data in various downstream planes. It is concluded that it is possible to compute using a RANS model quite well the spatially averaged flow close behind the VGs operating in a turbulent boundary layer.

The generated flow was further analyzed and validated against the PIV data. The main indicator for the validation procedure was the circulation of the velocity field. The circulation was computed directly from its integral definition and from fitting the numerical velocity profile to the Lamb-Oseen Vortex. The Reynolds-Stress turbulence model performed better than the k-ω SST and the Spalart-Allmaras models. For the rectangular configuration, the experimental and numerical circulation results remain constant and agree quite well up to the third downstream plane while in the rest of the planes the circulation decreases. For the triangular configuration, the circulation results agree for the two investigated planes. It can be summed up that the two investigated geometries have a comparable impact regarding the circulation of the velocity field even if they operate in a different way.

A hypothesis for the VGs case was verified. Specifically, the circulation in the wake was estimated as the summation of the trailed circulation from the lifting line theory. The bound circulation was estimated from the Kutta-Joukowski 2D airfoil theory while the local lift force from the integration of the pressure jump over the VG height. The resultant circulation in the wake was verified by comparing to the circulation coming from the definition and the Lamb-Oseen Vortex.

References

[1] C. M. Velte, C. Braud, S. Coudert, and J.-M. Foucaut, "Vortex generator induced flow in a high re boundary layer," *Journal of Physics: Conference Series (online)*, vol. 555, no. 1, p. 012102, 2014.

[2] P. K. Kundu, I. M. Cohen, and D. R. Dowling, *Fluid mechanics: Sixth edition*. Elsevier, 2015.

[3] CD-adapco, *STAR-CCM+ User Guide*. Siemens, 2016.

[4] M. Gentry and A. Jacobi, "Heat transfer enhancement by delta-wing-gene rated tip vortices in flat-plate and developing channel flows," *Journal of Heat Transfer-transactions of the Asme*, vol. 124, no. 6, pp. 1158–1168, 2002.

[5] M. O. L. Hansen, *Aerodynamics of wind turbines*. Earthscan Publications Ltd, 2015.

[6] G. Gyatt, "Development and testing of vortex generators for small horizontal axis wind turbines," *Renewable Energy*, p. 45p, 1986.

[7] C. C. Wang, J. Lo, Y. T. Lin, and C. S. Wei, "Flow visualization of annular and delta winlet vortex generators in fin-and-tube heat exchanger application," *International Journal of Heat and Mass Transfer*, vol. 45, no. 18, pp. 3803–3815, 2002.

[8] M. Koike, T. Nagayoshi, and N. Hamamoto, "Research on Aerodynamic Drag Reduction by Vortex Generators," *Package Engineering*, no. 2, pp. 11–16, 2004.

[9] R. E. Breidenthal and D. A. Russell, "Aerodynamics of Vortex Generators," Tech. Rep. December, 1988.

[10] J. C. Lin, *Review of research on low-profile vortex generators to control boundary layer separation*, vol. 38. 2002.

[11] C. M. Velte, M. O. L. Hansen, and V. L. Okulov, "Multiple vortex structures in the wake of a rectangular winglet in ground effect," *Experimental Thermal and Fluid Science*, vol. 72, pp. 31–39, 2016.

[12] A. Akcayoglu, "Flow past confined delta-wing type vortex generators," *Experimental Thermal and Fluid Science*, vol. 35, no. 1, pp. 112–120, 2011.

[13] L. Florentie, A. H. van Zuijlen, S. J. Hulshoff, and H. Bijl, "Effectiveness of Side Force Models for Flow Simulations Downstream of Vortex Generators," *AIAA Journal*, pp. 1–12, 2016.

[14] E. E. Bender, B. H. Anderson, and P. J. Yagle, "Vortex generator modeling for navier-stokes codes," *Proceedings of the 1999 3rd Asme/jsme Joint Fluids Engineering Conference, Fedsm'99, San Francisco, California, Usa, 18-23 July 1999 (cd-rom)*, p. 1, 1999.

[15] C. M. Velte, "Characterization of vortex generator induced flow," 2009.

[16] H. Versteeg, W. Malalasekera, and CFD, *Introduction to computational fluid dynamics.* Longman, 1995.

[17] CFD-ONLINE, "Meshing, Introduction, Mesh Classification." available at https://www.cfd-online.com/Wiki/Meshing.

[18] F. R. Menter, "Best Practice: Scale-Resolving Simulations in ANSYS CFD," *ANSYS Inc*, no. April, pp. 1–70, 2012.

[19] G. Batchelor, *An introduction to fluid dynamics.* Cambridge University Press., 1991.

[20] D. Wilcox, *Turbulence Modeling for CFD.* DCW Industries, 1994.

[21] F. Menter, "Two-equation eddy-viscosity turbulence modelling for engineering applications," *AAIA*, vol. 43, no. 329(8), pp. 1598–1605, 1994.

[22] P. Spalart and S. Allmaras, "A one-equation turbulence model for aerodynamic flows," *AAIA*, vol. 92, no. 0439, 1992.

[23] J. Lighthill, *An informal introduction to theoretical fluid mechanics*, vol. 2. Clarendon press, 1986.

[24] P. Saffman, *Vortex dynamics.* Cambridge University Press, 1992.

[25] N. N. Ahmad, F. H. Proctor, F. M. L. Duparcmeur, and D. Jacob, "Review of idealized aircraft wake vortex models," *52nd Aiaa Aerospace Sciences Meeting*, pp. 28 pp., 28 pp., 2013.

[26] S. Pope, *Turbulent Flows.* Cambridge University Press, 2003.

A. Appendix - Numerical Model

In this section of Appendix, additional Figures of the building procedure of the numerical model are provided.

Figure A.1 illustrates the geometry configuration of the TrD as derived from the CAD/-Geometry tool of Star CCM+.

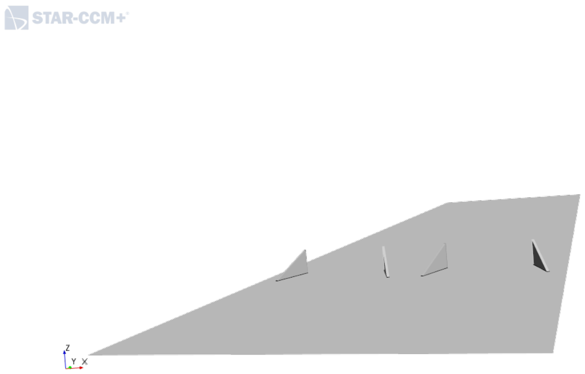

Figure A.1: Geometry scene of the triangular vanes

The block i.e surrounding walls created in order to enclosure the fluid flow domain is shown in Figure A.2

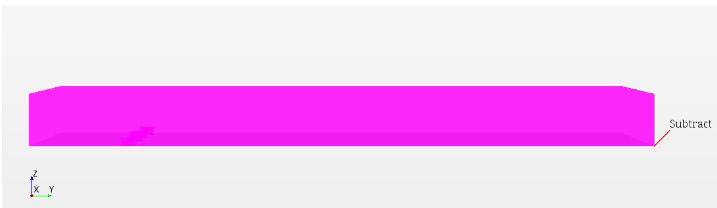

Figure A.2: Surrounding walls of the wind tunnel floor

The polyhedral cell option used in order to generate the mesh for both ReD and TrD is shown in Figure (A.3).

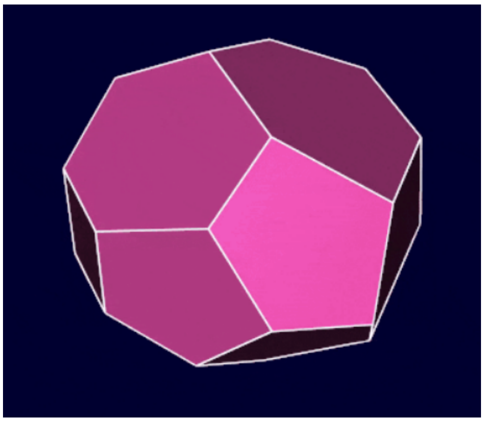

Figure A.3: A polyhedral-shaped cell [3]

The refinement area for the TrD configuration is shown in Figure A.4. It is generated up to 12h downstream since the comparison with the experimental data is conducted up to this position.

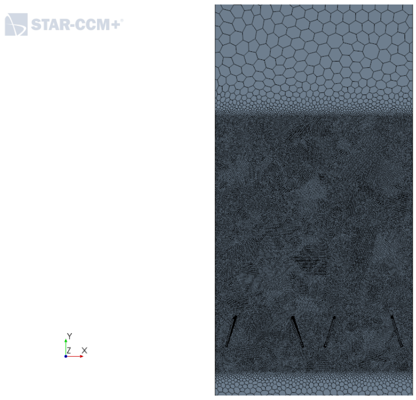

Figure A.4: Top view of the generated mesh for the TrD configuration

The properties of the MBAR-414-33-20D DTU personal computer used in order to generate the mesh is presented in table A.1 below.

Table A.1: Properties of the PC used for the mesh generation

PC properties

Processor	Intel Core i7-3770 CPU @3.4 GHz
Installed Memory (RAM)	16 GB
System type	64-bit Operating System

B. Appendix - Results

The velocity components of the results are provided in this section.

B.1. y and z velocity components for the RST turbulence model (ReD)

The comparison between the experimental and numerical velocity fields in y-direction and z-direction in the downstream planes (12h,25h,40h,50h) is illustrated in Figures B.1 to B.8 below.

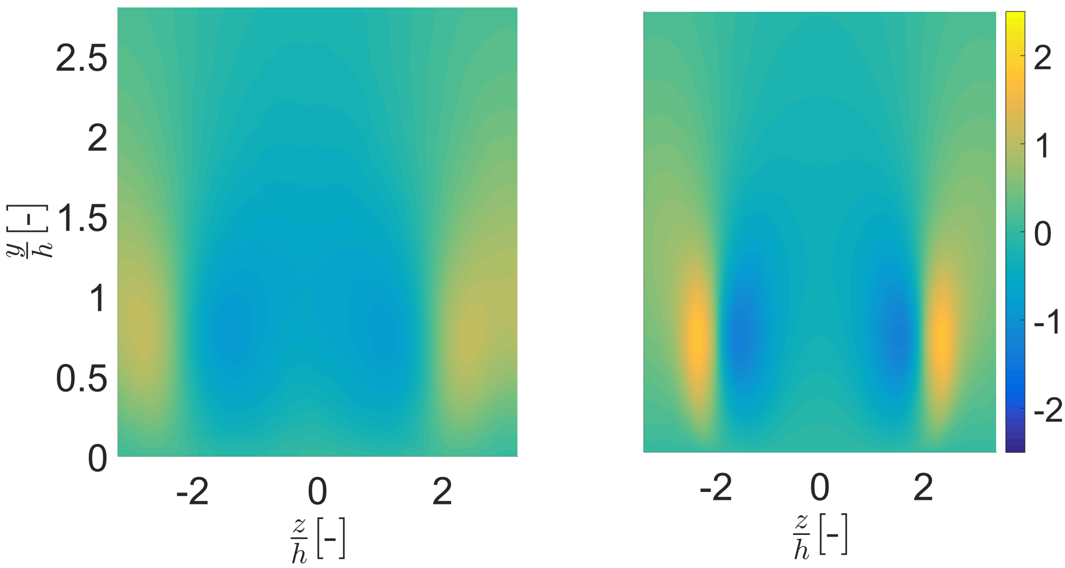

Figure B.1: Comparison between the experimental (left) and computational (right) vertical velocity components (y-direction) 12h downstream of the VGs

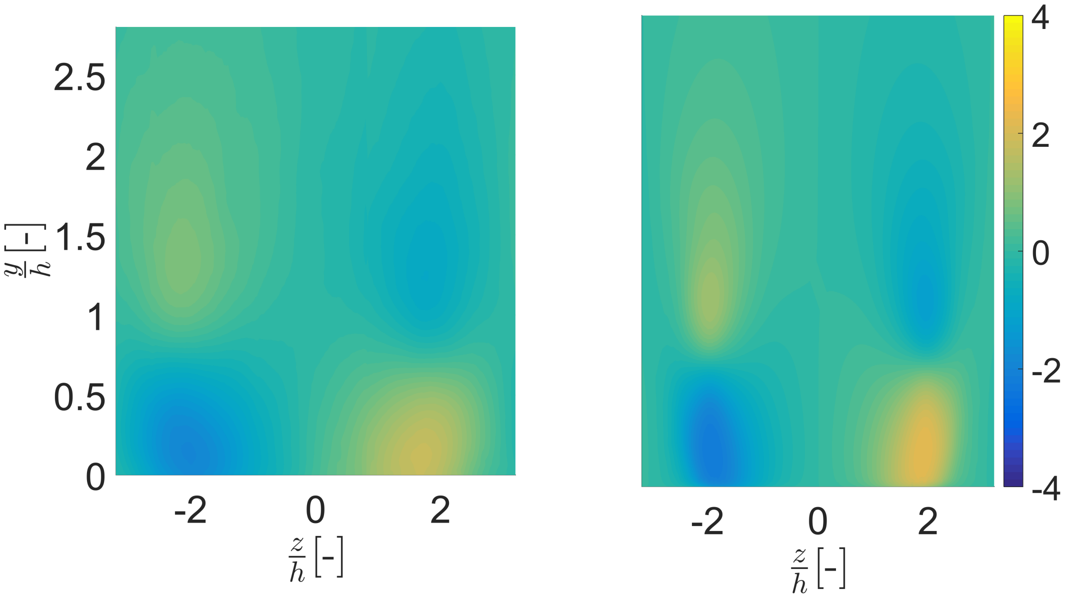

Figure B.2: Comparison between the experimental (left) and computational (right) lateral velocity components (z-direction) 12h downstream of the VGs

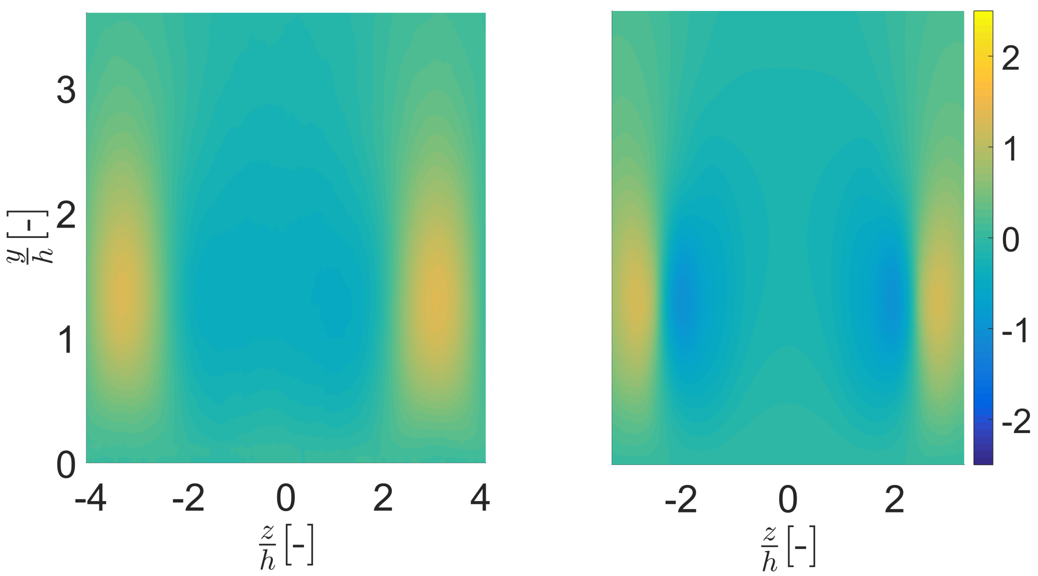

Figure B.3: Comparison between the experimental (left) and computational (right) vertical velocity components (y-direction) 25h downstream of the VGs

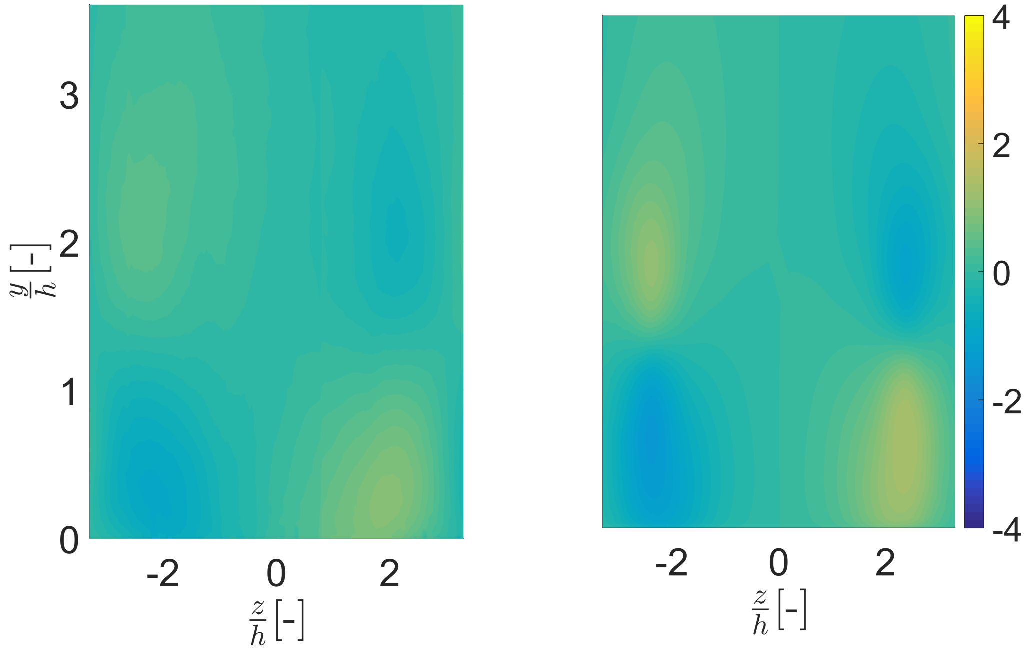

Figure B.4: Comparison between the experimental (left) and computational (right) lateral velocity components (z-direction) 25h downstream of the VGs

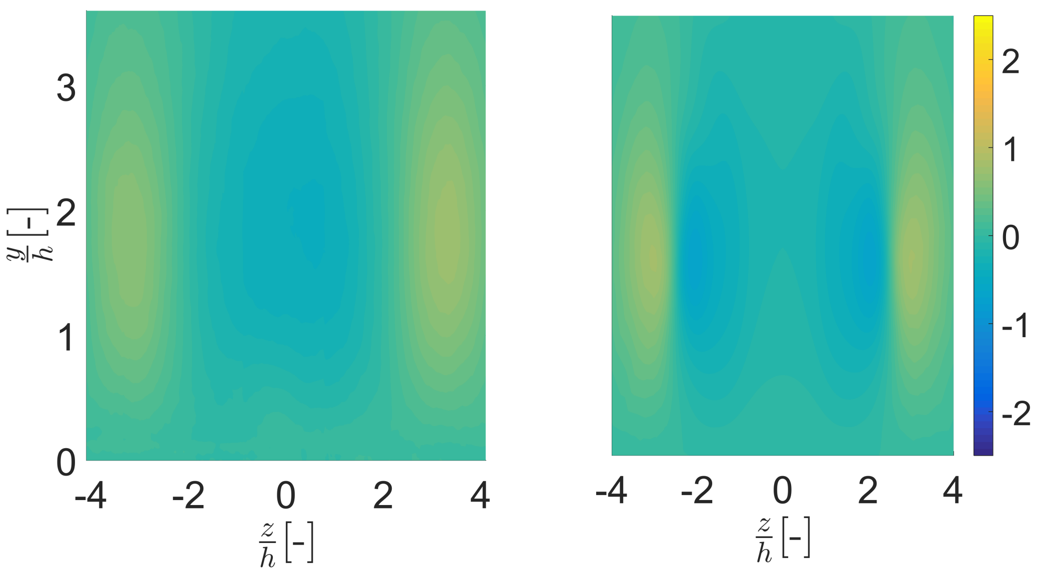

Figure B.5: Comparison between the experimental (left) and computational (right) vertical velocity components (y-direction) 40h downstream of the VGs

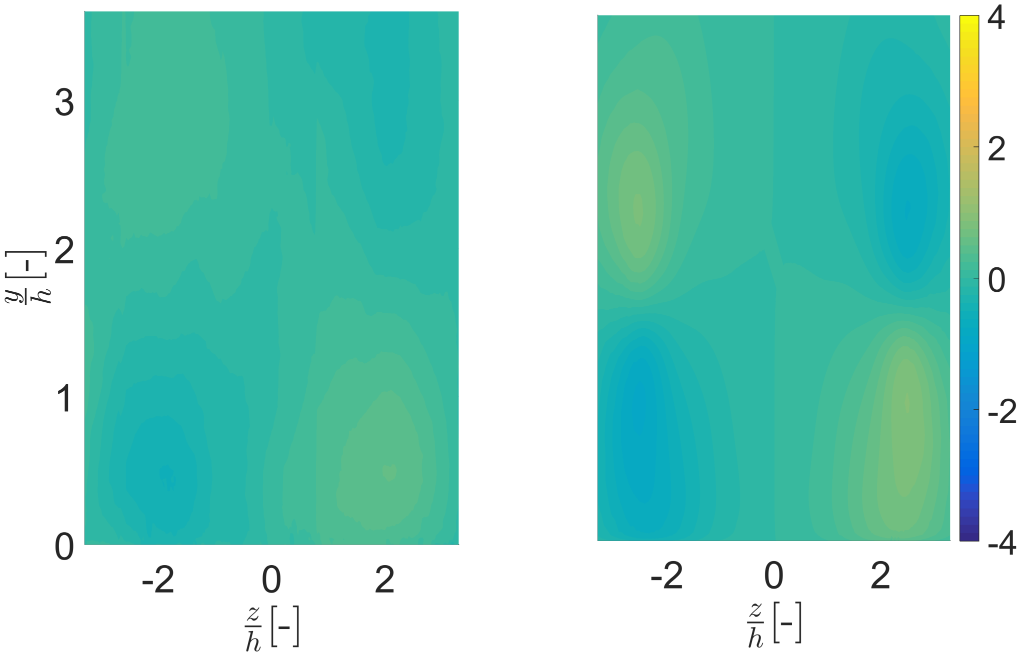

Figure B.6: Comparison between the experimental (left) and computational (right) lateral velocity components (z-direction) 40h downstream of the VGs

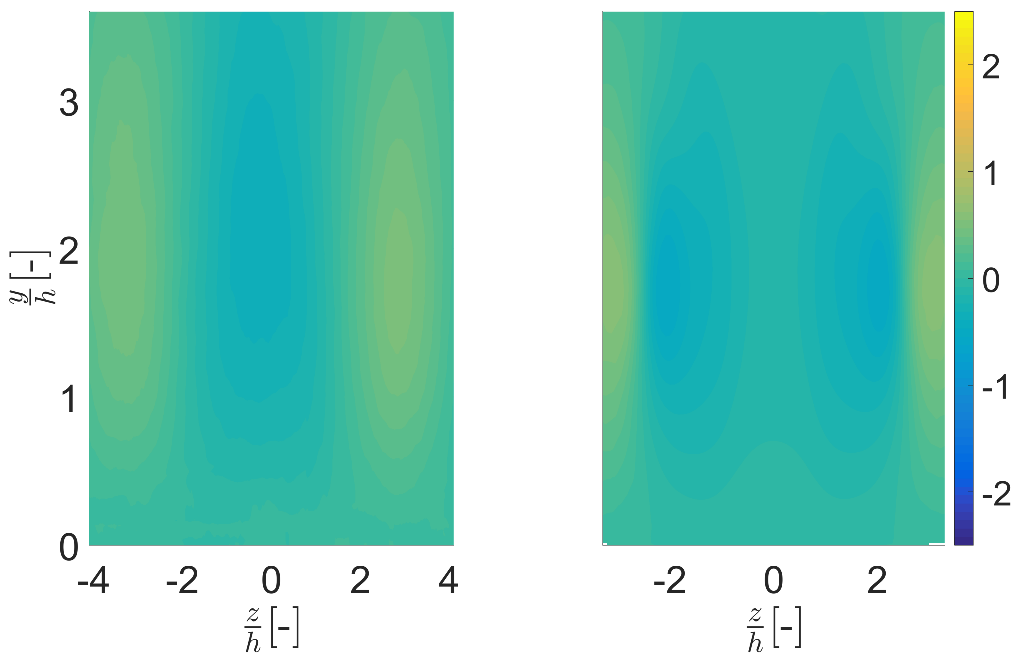

Figure B.7: Comparison between the experimental (left) and computational (right) vertical velocity components (y-direction) 50h downstream of the VGs

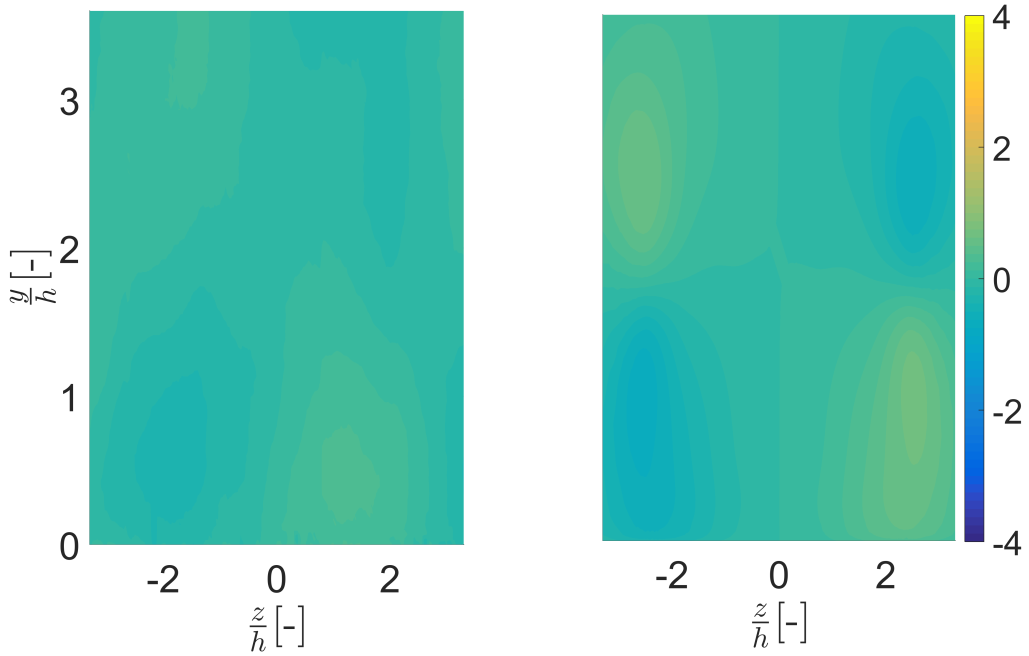

Figure B.8: Comparison between the experimental (left) and computational (right) lateral velocity components (z-direction) 50h downstream of the VGs

B.2. y and z velocity components for the RST turbulence model (TrD)

The vertical and lateral velocity components at 12h downstream for the TrD configuration are illustrated in Figures B.9

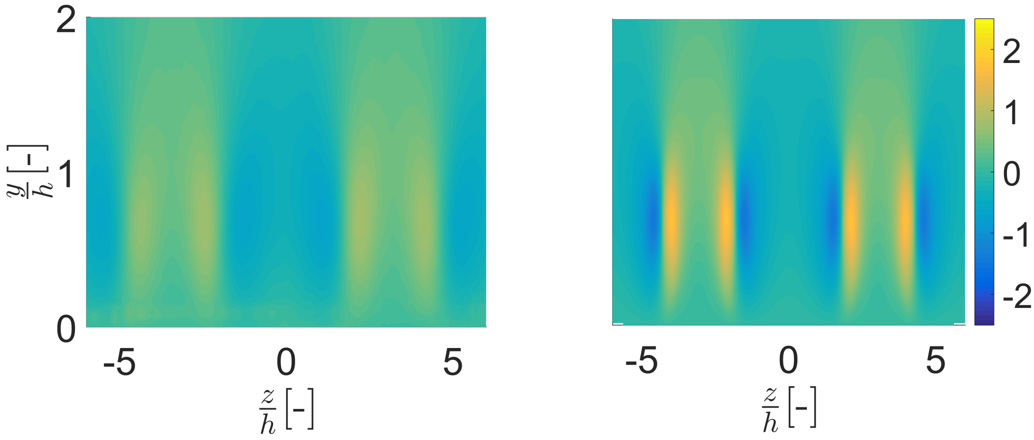

Figure B.9: Comparison between the experimental (left) and computational (right) vertical velocity components (y-direction) 12h downstream of the VGs (TrD)

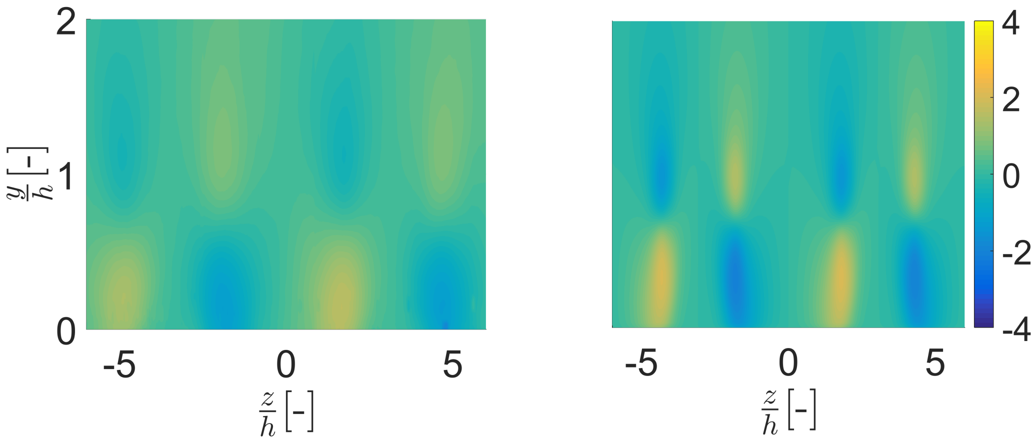

Figure B.10: Comparison between the experimental (left) and computational (right) lateral velocity components (z-direction) 12h downstream of the VGs (TrD)

C. Appendix - Validation

In this section of Appendix, additional Figures and further explanations for the fourth chapter are provided.
In the following Figure (C.1) the vortex is distinct and the location of the vortex center is defined.

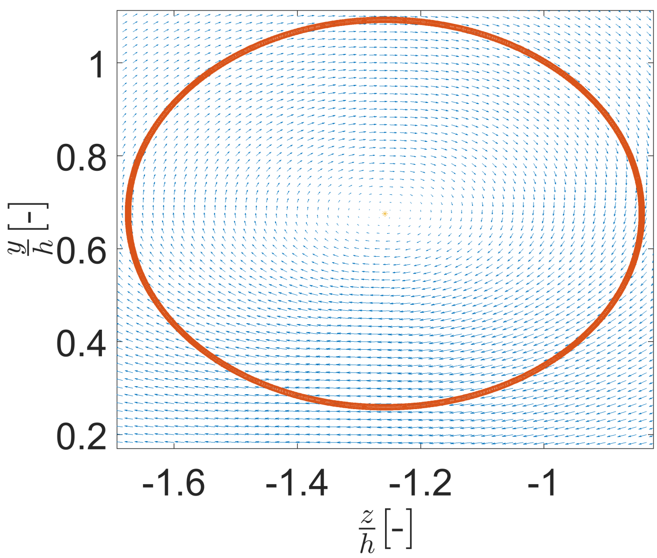

Figure C.1: Zoomed-in plot of Figure 5.2

The transformation from the Cartesian to polar coordinate system is visually described in Figure C.2.

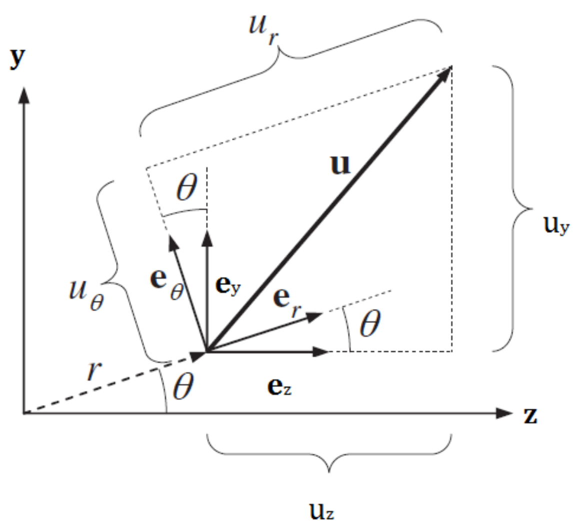

Figure C.2: Transformation from Cartesian to polar coordinate system [2]

C.1. Lamb-Oseen

Figure C.3 corresponds to the fit between the numerical and LOV velocity profiles at 40h downstream.

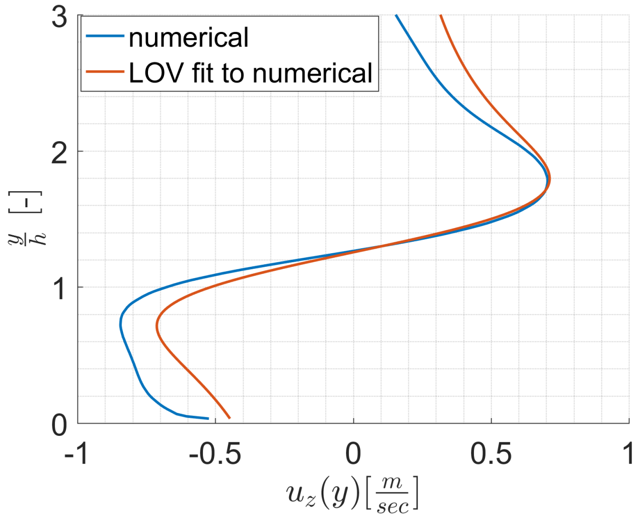

Figure C.3: Determination of Γ with the use of Lamb-Oseen vortex at 40h downstream

D. Appendix - Hypothesis for the VGs

The aspect ratio for the rectangular and triangular devices can be observed in Figure D.1. For the rectangular is equal to $\frac{2h}{L_{VG}}$ and for the delta winglet is equal to $\frac{4h}{L_{VG}}$

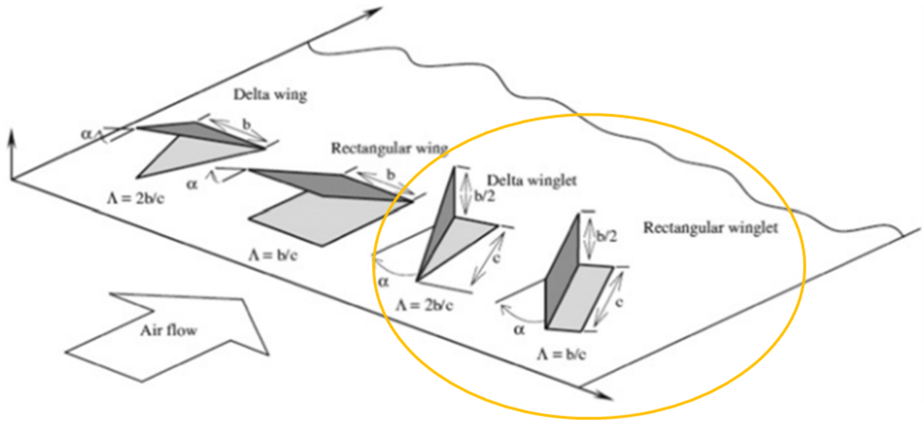

Figure D.1: Aspect ration for the rectangular and triangular winglets [4]

E. Appendix - Presentation in WESC 2017

The presentation in WESC 2017 is provided in this section of the Appendix.

Verification of numerical modelling of VG flow by comparing to PIV data and analyzing the production of wake circulation

Antonis Charalampous[1], Martin O. L. Hansen[1], Clara M.Velte[2]
[1]DTU Wind Energy
[2]DTU Mechanical Engineering

DTU Wind Energy
Department of Wind Energy

Background

Clara Velte previously made PIV measurements on VGs in the wind tunnel in Lille (France) in a turbulent boundary layer to measure the flow at realistic operating conditions

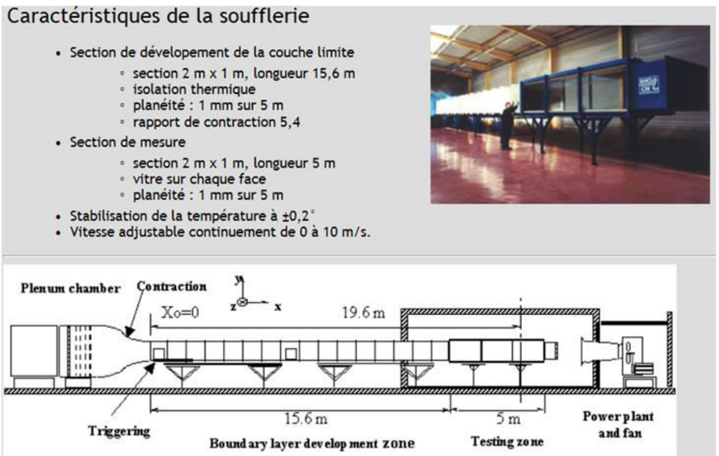

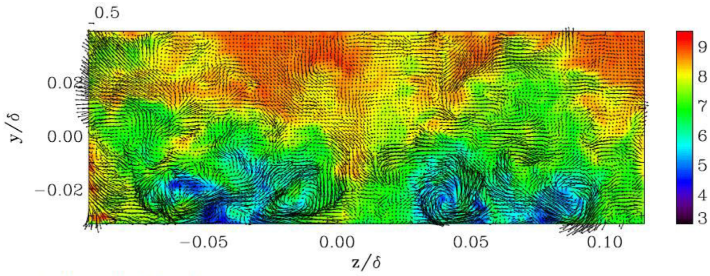

Figure 2 Example of result.

In the work presented here these data are used for CFD validation and testing of a proposed engineering model for designing VGs

Geometries

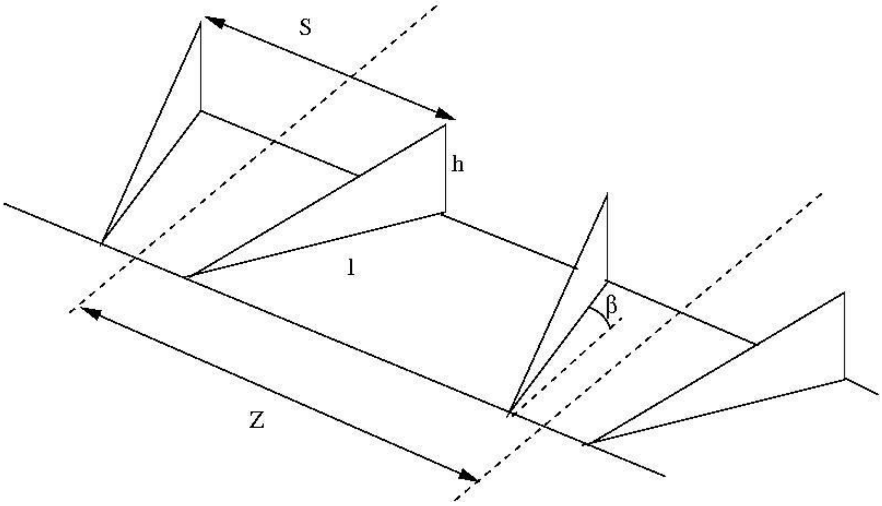

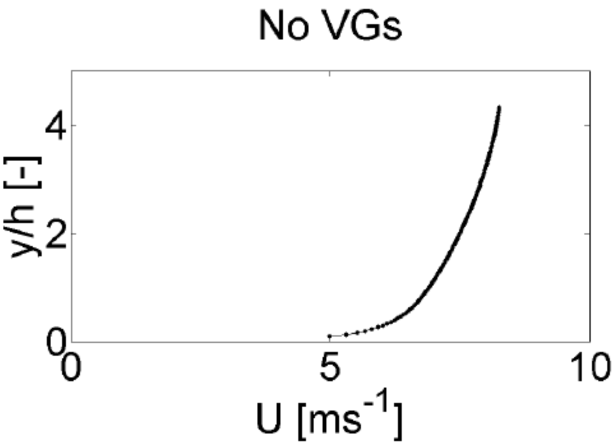

Geometry (Rectangular and triangular):
h=0.06 m, l=2h=0.12m, Z/h=6, S/h=2.5

$$\mathrm{Re}_l = 64000$$

Numerical model

1)11e6 polyhedral cells

2) 20 prism layers

3) Several RANS turbulent models tested

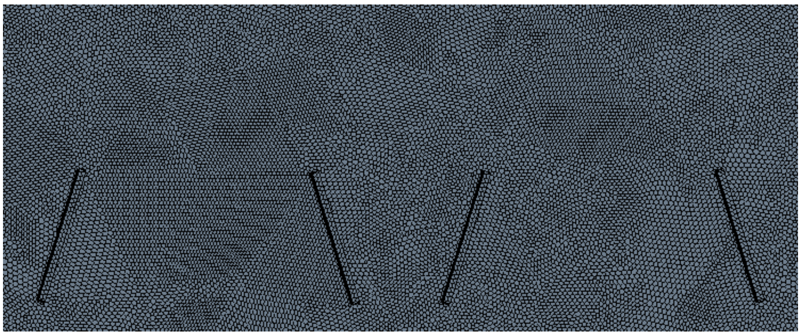

Top view of the mesh scene

Stream wise velocity

The snapshots measured with PIV were averaged and compared to CFD (RANS) at various downstream planes and a quite good qualitative agreement is seen

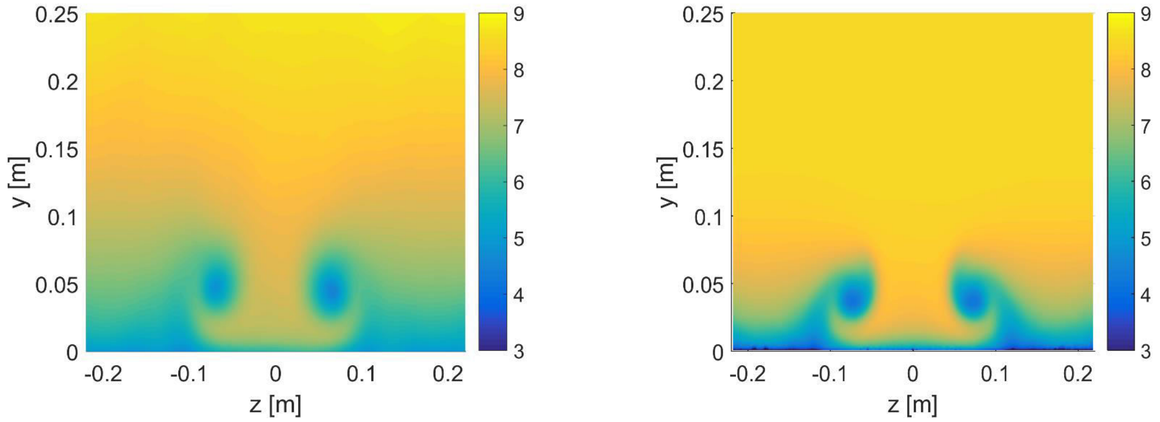

Comparison between experimental (left) and numerical (right) streamwise velocity component in a plane 3 VG heights behind VGs. The Reynolds-Stress Turbulence Model was used here.

Determination of circulation in wake

1) Direct use of definition

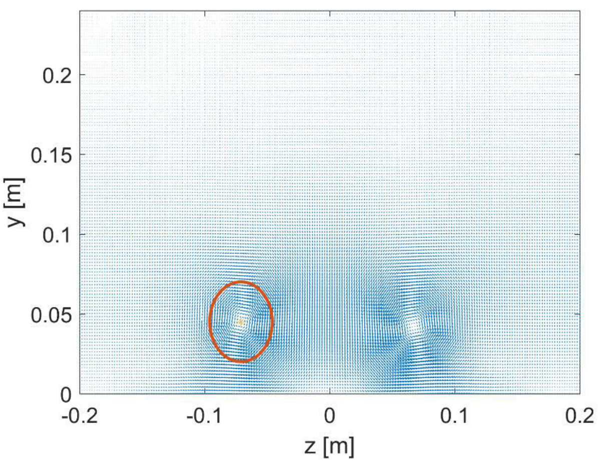

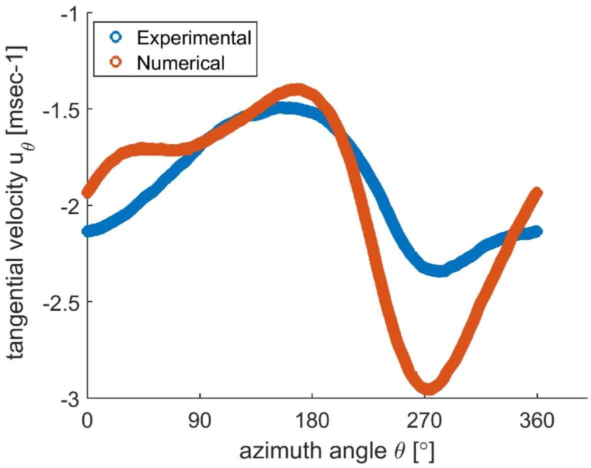

$$\Gamma = \oint_{0°}^{360°} u_{\boldsymbol{\theta}} r \, d\theta$$

Experimental: Γ = -0.3 m^2sec^{-1}
Numerical: Γ = -0.31 m^2sec^{-1}

Determination of circulation in wake

2) Lamb Oseen vortex

$$u_z = \sum \frac{-(y_p - y_{vortex})\Gamma}{2\pi r^2}\left(1 - \exp\left(-\left(\frac{r}{\varepsilon}\right)^2\right)\right)$$

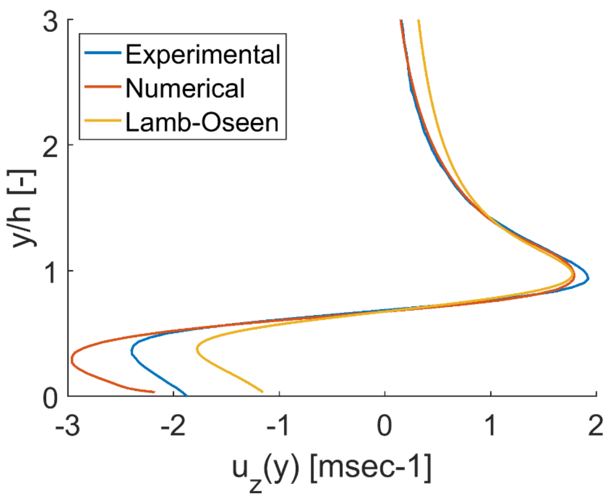

Γ=-0.28 m^2sec^{-1}

Hypothesis

Does the circulation in the wake correlate with the bound circulation as on a conventional wing ?

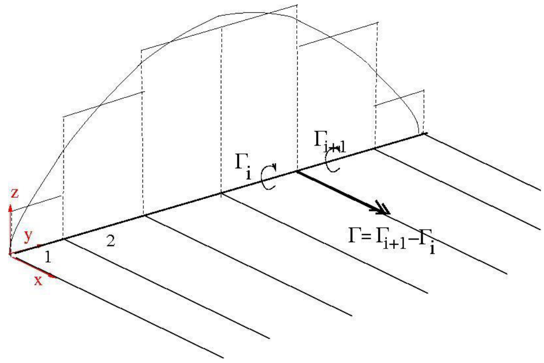

Conventional (numerical) lifting line model. The local trailed circulation is the change of bound circulation to fulfill Helmholtz's theorems.

Next we assume the VGs to behave as a wing (even though the aspect ratio is really low) and relate the local circulation to the local lift using Kutta-Joukowski theorem as

$$l(y) = \rho U(y)\Gamma(y) \quad [\mathrm{N/m}]$$

y being the distance from the surface where the VG is mounted

The load [N/m] at a height y was determined by integrating the net pressure distribution along x as

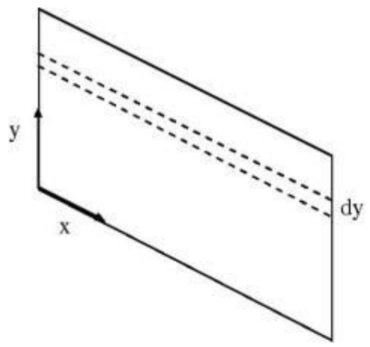

$$f(y) = \int_0^l \Delta p(x, y)\,dx$$

A rectangular VG

Since the pressure force is acting normal to the surface this load is projected normal to the inflow to estimate the lift

$$l(y) \approx f(y)\cos\beta$$

Determination of bound circulation

From the local lift, the bound circulation distribution was estimated at 17 heights and taking into account the local velocity at each height:

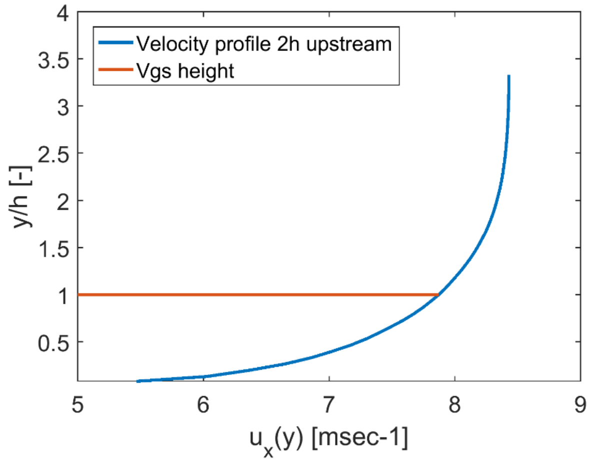

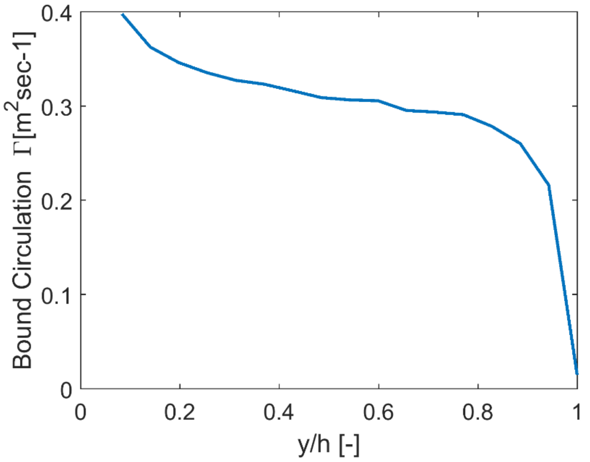

Determination of trailed circulation

Assuming that the VG behaves approximately as a lifting line the trailed circulation can be calculated in the indermediate heights as $\Gamma = \Gamma_{i+1} - \Gamma_i$

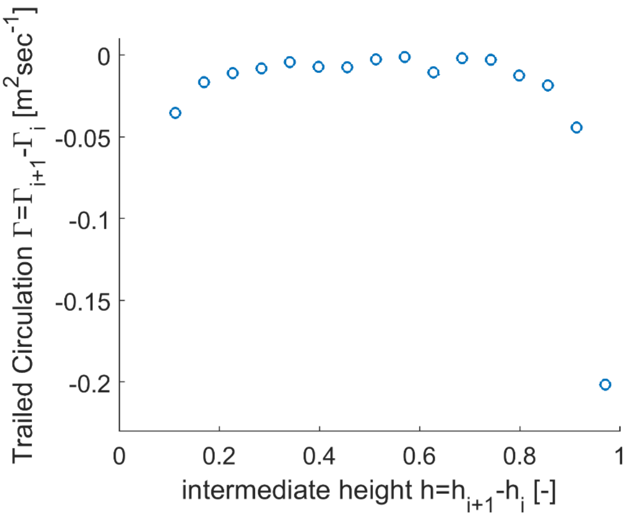

Trailed circulation from the mid-height to the tip:

Γ=-0.295 m^{2}sec^{-1}

Conclusion

1) It is possible to compute using RANS quite well the spatially averaged flow behind a VG operating in a turbulent BL

2) The produced circulation in the wake was computed directly from its definition and from fitting the vertical velocity profile to a Lamb-Oseen vortex

3) A hypothesis was verified where the wake circulation was estimated as the sum of the trailed circulation computed (curled up) from simple lifting line theory and where the bound circulation was computed from Kutta-Joukowski airfoil theory and the the local lift from integrating the pressure jump over the VG

DTU Wind Energy is a department of the Technical University of Denmark with a unique integration of research, education, innovation and public/private sector consulting in the field of wind energy. Our activities develop new opportunities and technology for the global and Danish exploitation of wind energy. Research focuses on key technical-scientific fields, which are central for the development, innovation and use of wind energy and provides the basis for advanced education at the education.

We have more than 240 staff members of which approximately 60 are PhD students. Research is conducted within nine research programmes organized into three main topics: Wind energy systems, Wind turbine technology and Basics for wind energy.

Technical University of Denmark
Department of Wind Energy
Frederiksborgvej 399
4000 Roskilde Denmark
Telephone 46 77 50 85

info@vindenergi.dtu.dk
www.vindenergi.dtu.dk